Missing-In-Metastasis / Metastasis Suppressor 1 regulates B cell receptor signaling, B cell metabolic potential and T cell-independent immune responses

Alexey V Sarapulov[1,2], Petar Petrov[1,2], Sara Hernández-Pérez[1,2,], Vid Šuštar[1], Elina Kuokkanen[1], Rufus Vinod[1], Marika Vainio[1,2], Lena Cords[3], Marco Fritzsche[3, 4], Yolanda R Carrasco[5], and Pieta K Mattila[1,2*]

[1] Institute of Biomedicine and MediCity Research Laboratories, University of Turku, Turku, Finland
[2] Turku Bioscience, University of Turku and Åbo Akademi University, Turku, Finland
[3] MRC Human Immunology Unit, Weatherall Institute of Molecular Medicine, University of Oxford, Oxford, UK
[4] Kennedy Institute for Rheumatology, University of Oxford, Oxford, UK
[5] Department of Immunology and Oncology, Centro Nacional de Biotecnología (CNB)-CSIC, Madrid, Spain

*** Correspondence:**
Corresponding author
Pieta K Mattila
pieta.mattila@utu.fi

Keywords: MIM, MTSS1, I-BAR domain protein, BCR, B cell receptor signaling, B cell activation, actin cytoskeleton, immune response, adaptive immune response, TLR, metabolism

Manuscript contains five main figures and one table (reagents). Word count: ~10000.

Abstract

Efficient generation of antibodies by B cells is one of the prerequisites of protective immunity. B cell activation by cognate antigens via B cell receptors (BCR), or pathogen-associated molecules through pattern-recognition receptors, such as Toll-like receptors (TLRs), leads to transcriptional and metabolic changes that ultimately transform B cells into antibody producing plasma cells or memory cells. BCR signaling and a number of steps downstream of it rely on coordinated action of cellular membranes and the actin cytoskeleton, tightly controlled by concerted action of multiple regulatory proteins, some of them exclusive to B cells. Here, we dissect the role of Missing-In-Metastasis (MIM), or Metastasis suppressor 1 (MTSS1), a cancer-associated membrane and actin cytoskeleton regulating protein, in B cell-mediated immunity by taking advantage of MIM knockout mouse strain. We show undisturbed B cell development and largely normal composition of B cell compartments in the periphery. Interestingly, we found that $MIM^{-/-}$ B cells are defected in BCR signaling in response to surface-bound antigens but, on the other hand, show increased metabolic activity after stimulation with LPS or CpG. *In vivo*, MIM knockout animals exhibit impaired IgM antibody responses to immunization with T cell-independent antigen. This study provides the first comprehensive characterization of MIM in B cells, demonstrates its regulatory role for B cell-mediated immunity, as well as proposes new functions for MIM in tuning receptor signaling and cellular metabolism, processes which may also contribute to the poorly understood functions of MIM in cancer.

1 Introduction

Adaptive immune responses, such as efficient clearing of pathogens while maintaining the homeostasis of the host, depend on fine-tuned balance of various signals. Increasing evidence points towards an important role of the actin cytoskeleton and plasma membrane organization at the cross-roads of various signaling pathways orchestrating lymphocyte action (Mattila et al., 2016). In B cells, the actin cytoskeleton enables changes in cell morphology, required, for instance, during the formation of the immunological synapse (Kuokkanen et al., 2015). Interestingly, actin cytoskeleton and plasma membrane also potently regulate B cell receptor (BCR) signaling (Treanor et al., 2010; Mattila et al., 2013, 2016). A plethora of cytoskeletal regulator proteins enable the multifaceted roles of the actin cytoskeleton in living cells. Lymphocytes generally present very characteristic protein expression patterns and considering the specialized functions of these immune cells, it is not surprising that this also holds true for the regulators of the actin cytoskeleton. One best-known example of such protein is Wiscott-Aldrich syndrome (WAS) protein (WASp), a critical regulator of lymphocyte function and an activator of Arp2/3 actin filament (F-actin) nucleator complex (Bosticardo et al., 2009).

A highly conserved, cancer-associated protein linked to the regulation of both the actin cytoskeleton and the plasma membrane, Missing in Metastasis (MIM) or Metastasis Suppressor 1 (MTSS1), is highly expressed in spleen and particularly in B cells (Mattila et al., 2003; BioGPS.org portal). MIM belongs to a family of proteins with a characteristic inverse Bin, Amphiphysin, Rvs (I-BAR) domain, or IRSp53 and MIM homology domain (IMD), which binds and deforms cellular membranes (Mattila et al., 2007; Safari and Suetsugu, 2012). It also directly interacts with and regulates actin via its C-terminal WASp homology 2 (WH2) domain (Mattila et al., 2003; Woodings et al., 2003) and indirectly via interactions with other actin regulatory proteins, such as cortactin and Rac1 GTPase (Mattila et al., 2003, 2007; Lin et al., 2005; Cao et al., 2012). MIM has also been shown to regulate bone marrow and lymphoid cell trafficking presumably through regulation of CXCR4 internalization as seen in cancer cell lines (Yu et al., 2012; Zhan et al., 2016; Li et al., 2017; Zhao et al., 2019). Importantly, MIM has been linked to various cancers, either as a putative tumor metastasis suppressor, or promoter (Machesky and Johnston, 2007). Genetic alterations in *MIM/MTSS1* gene were found in 6% of sequenced cancer samples and, depending on the cancer type, both diminished or increased gene expression profiles are seen (Petrov et al., 2019). Regarding hematopoietic malignancies, MIM is upregulated, for example, in hairy cell and mantle cell lymphomas as well as chronic lymphocytic leukaemia (CLL). In CLL, interestingly, the good prognosis samples exhibit highest levels of MIM while the poor prognosis samples show lower MIM levels in comparison to good prognosis samples (Petrov et al., 2019). In mice, it has been reported that upon aging MIM knockout animals develop lymphomas resembling diffuse large B cell lymphoma (DLBCL) (Yu et al., 2012). Moreover, a degenerative kidney disease, potentially linked to impaired cell-cell junction formation, as well as a defected dendritic spine formation and neuronal alterations have been reported in MIM knockout mice (Saarikangas et al., 2011, 2015). These findings illustrate the complexity of MIM function, the basis of which remains enigmatic due to the lack of understanding about the molecular mechanisms and connected pathways. Despite the reported high expression in B cells and the association with hematopoietic malignancies, nothing is known about the role of MIM in activation of adaptive immune responses.

In this study, we took advantage of a MIM knockout mouse model ($MIM^{-/-}$, MIM-KO) (Saarikangas et al., 2011) to explore the physiological role of MIM in B cell compartment, specifically in early B cell activation and mounting of the antibody responses. While we found no defects in B cell development, MIM-deficiency caused a variety of changes in mature B cells. $MIM^{-/-}$ B cells showed significantly reduced signaling upon stimulation with surface-bound antigens mimicking activation via immunological synapse. T cell-independent IgM responses were reduced in $MIM^{-/-}$ mice, while on the other hand, T cell-dependent immune responses appeared normal. Unlike BCR stimulation, $MIM^{-/-}$ B cells were robustly activated by TLR agonists that, interestingly, also led to increased metabolic activity

98 in cells lacking MIM. Our study highlights the complex role of MIM in different cellular functions and
99 can serve as a stepping stone for unveiling the role of MIM in hematopoietic cancers.
100

101 # 2 Materials and Methods

102 ## 2.1 Antibodies and chemicals

103 List of antibodies and reagents used in the study can be found in Table I.

104 Table 1. Key reagents table

Name	Catalog #	Company	Application
AffiniPure Donkey Anti-Mouse IgM, μ Chain Specific	715-005-020	Jackson ImmunoResearch	Stimulatory antibodies
AffiniPure F(ab´)$_2$ Fragment Donkey Anti-Mouse IgM	715-006-020	Jackson ImmunoResearch	Stimulatory antibodies
AF647 AffiniPure F(ab´)$_2$ Fragment Donkey Anti-mouse IgM	715-606-020	Jackson ImmunoResearch	Stimulatory antibodies
Monobiotinylated Purified Rat anti-mouse Ig κ light chain	559749 or 21343	BD Biosciences or Thermo Fisher Scientific	Stimulatory antibodies
Purified Rat Anti-Mouse IgM - Clone II/41 (RUO)	553435	BD Biosciences	ELISA, capture antibody
AffiniPure Goat Anti-Mouse IgG, Fcγ Fragment Specific	115-005-071	Jackson ImmunoResearch	ELISA, capture antibody
Goat Anti-Mouse IgG1-BIOT	1071-08	SouthernBiotech	ELISA, detection antibody
Goat Anti-Mouse IgG2b-BIOT	1091-08	SouthernBiotech	ELISA, detection antibody
Goat Anti-Mouse IgG2c-BIOT	1078-08	SouthernBiotech	ELISA, detection antibody
Goat Anti-Mouse IgG3, Human/Bovine/Horse SP ads-BIOT	1103-08	SouthernBiotech	ELISA, detection antibody
Goat Anti-Mouse IgG Fc-BIOT	1033-08	SouthernBiotech	ELISA, detection antibody
Biotin Rat Anti-Mouse IgM, Clone R6-60.2 (RUO)	553406	BD Biosciences	ELISA, detection antibody
C57BL/6 Mouse Immunoglobulin Panel	5300-01B	SouthernBiotech	ELISA, standard
Purified Rat Anti-Mouse CD16/CD32	553142	BD Biosciences	Flow cytometry, Fc-block
FITC Rat Anti-Mouse IgG1	553443	BD Biosciences	Flow cytometry, CSR
FITC Rat Anti-Mouse IgG2b	553395	BD Biosciences	Flow cytometry, CSR
FITC Rat Anti-Mouse IgG3	553403	BD Biosciences	Flow cytometry, CSR
AffiniPure Goat anti-Mouse IgG2c, FITC-conjugated	115-095-208	Jackson ImmunoResearch	Flow cytometry, CSR
LPS, Lipopolysaccharides from Escherichia coli	L2887-5MG	Sigma-Aldrich	CSR, Metabolism
CpG ODN 1826	tlrl-1826	Invivogen	Metabolism
CD40L, Recombinant Mouse CD40 Ligand/TNFSF5 (HA-tag)	8230-CL-050	R&D Systems	CSR
IL-4, Recombinant Mouse IL-4	404-ML-010	R&D Systems	CSR, Metabolism
IFNγ, Recombinant Mouse IFN-g	575304	BioLegend	CSR
TGF-β, Recombinant Mouse TGF-beta 1	7666-MB-005	R&D Systems	CSR
BD Horizon™ V450 Rat Anti-Mouse IgM Clone R6-60.2	560575	BD Biosciences	Flow cytometry
AF488 anti-mouse IgD [11-26c.2a]	405718	Biolegend	Flow cytometry
AF700 anti-mouse CD19 [6D5]	115528	Biolegend	Flow cytometry
APC anti-mouse CD19 [6D5]	115512	Biolegend	Flow cytometry
APC/Cy7 anti-mouse/human CD45R/B220 [RA3-6B2]	103224	Biolegend	Flow cytometry
APC anti-mouse CD21/CD35 (CR2/CR1) [7E9]	123412	Biolegend	Flow cytometry
Alexa Fluor® 594 anti-mouse CD23 [B3B4]	101628	Biolegend	Flow cytometry
PE anti-mouse CD93 (AA4.1, early B lineage) [AA4.1]	136503	Biolegend	Flow cytometry
PE anti-mouse CD3e [145-2C11]	100308	Biolegend	Flow cytometry
FITC anti-mouse CD4 [GK1.5]	100406	Biolegend	Flow cytometry
APC anti-mouse CD5 [53-7.3]	100626	Biolegend	Flow cytometry
Tom20 (FL-145)	sc-11415	Santa Cruz Biotechnology	Flow cytometry, metabolism
Goat anti-Rabbit IgG (H+L), AF488	A-11008	Thermo Fisher Scientific	Flow cytometry, metabolism
MTSS1 (P549) Ab	4385S	Cell Signaling Technologies	Immunoblotting
MTSS1 (N747) Ab	4386S	Cell Signaling Technologies	Immunoblotting
Phospho-Zap-70 (Tyr319)/Syk (Tyr352) Ab	2701P	Cell Signaling Technologies	Immunoblotting,

			microscopy
Syk (D3Z1E) XP¬ Rabbit mAb	13198S	Cell Signaling Technologies	Immunoblotting
Phospho-Lyn (Tyr507) Ab	2731P	Cell Signaling Technologies	Immunoblotting
Lyn (C13F9) rabbit mAb	2796S	Cell Signaling Technologies	Immunoblotting
Phospho-CD19 (Tyr531) Ab	3571S	Cell Signaling Technologies	Immunoblotting
CD19 Ab	3574S	Cell Signaling Technologies	Immunoblotting
Phospho-PI3 Kinase p85 (Tyr458)/p55 (Tyr199) Ab	4228S	Cell Signaling Technologies	Immunoblotting
Phospho-CD19 (Tyr531) Ab	3571S	Cell Signaling Technologies	Immunoblotting
Phospho-Akt (Ser473) (193H12) Rabbit mAb	4058S	Cell Signaling Technologies	Immunoblotting
Akt1 (C73H10) Rabbit mAb	2938S	Cell Signaling Technologies	Immunoblotting
Phospho-NF-kappa-B p65 (Ser536) (93H1) Rabbit mAb	3033S	Cell Signaling Technologies	Immunoblotting
NF-κB p65 (D14E12) XP® Rabbit mAb	8242S	Cell Signaling Technologies	Immunoblotting
p44/42 MAPK (Erk1/2) Ab	9102S	Cell Signaling Technologies	Immunoblotting
Phospho-p44/42 MAPK (Erk1/2) (Thr202/Tyr204) Ab	9101S	Cell Signaling Technologies	Immunoblotting
Phospho-Btk (Tyr223) (D1D2Z) Rabbit mAb	87457	Cell Signaling Technologies	Immunoblotting
Peroxidase AffiniPure Goat Anti-Rabbit IgG (H+L)	111-035-144	Jackson ImmunoResearch	Immunoblotting
Peroxidase AffiniPure Goat Anti-Mouse IgG, Fcγ Specific Ab	115-035-071	Jackson ImmunoResearch	Immunoblotting
Donkey Anti-Rabbit IgG Ab, IRDye 800CW Conjugated	926-32213	LI-COR Biosciences	Immunoblotting
AF555 Phalloidin	A34055	Thermo Fisher Scientific	Microscopy
AF647 anti-mouse/human CD45R/B220 Ab	103229	BioLegend	Microscopy
Anti-Phosphotyrosine Ab, clone 4G10®	05-321	Merck Miilipore	Microscopy
FITC Rat Anti-Mouse IgG2b	553395	BD	Microscopy
CXCL13	250-24-5ug	PeproTech	Microscopy, SLB
AlexaFluor 488 Mouse Anti-Btk (pY223)/Itk (pY180)	564847	BD Biosciences	Microscopy
Donkey anti-rabbit IgG, AF488 conjugate	A-21206	Thermo Fisher Scientific	Microscopy

2.2 Mice

MIM knockout mouse colony was a kind gift from Prof. Pekka Lappalainen and Dr. Pirta Hotulainen from the University of Helsinki and Minerva Foundation Institute for Medical Research (Saarikangas et al., 2011). The strain, in C57Bl/6 background, had no apparent health problems until the age of 8 months when mice were latest sacrificed, however, we observed that from all genotyped animals that were kept alive, 18 pups developed hydrocephaly over the study period. Among them, 17 were knockout, 1 heterozygote, and none wild-type. To generate this strain, Saarikangas et al (Saarikangas et al., 2011) introduced a *Neo*-cassette, containing several stop codons, by homologous recombination into Exon 1 of *MIM*/*Mtss1* gene in 129/Sv ES-cells. Chimeric mice were backcrossed to C57Bl/6J background for several generations and the colony in Turku was established by breedings of heterozygote founder animals. All experiments were done with age- and sex-matched animals and WT littermate controls were used whenever possible.

2.3 Immunizations

At the age of 3-4 months, groups of WT and *MIM*$^{-/-}$ females were immunized with NP_{40}-FICOLL (F-1420, Biosearch Technologies) for T-independent (TI) immunization or NP_{31}-KLH (N-5060, Biosearch Technologies) for T-dependent (TD) immunization. Each mouse received 50 µg of antigen in 150 µL of PBS (NP_{40}-FICOLL) or PBS/Alum (77161, Thermo Fisher) adjuvant (2:1 ratio) (NP_{31}-KLH) solution by intraperitoneal injection. Blood (~100 µL) was sampled from lateral saphenous veins on day -1 (preimmunization) and every week after immunization on days +7, +14, +21 and +28 for both FICOLL and KLH cohorts. Secondary immunization of KLH cohort was performed on day +135 (0) and blood was sampled on days +134 (-1), +139 (+4), +143 (+8) and +150 (+15). Coagulated blood was spun at +4°C / 2000 rpm for 10 min and serum was collected and stored at -20°C.

All animal experiments were approved by the Ethical Committee for Animal Experimentation in Finland. They were done in adherence with the rules and regulations of the Finnish Act on Animal Experimentation (62/2006) and were performed according to the 3R-principle (animal license numbers: 7574/04.10.07/2014, KEK/2014-1407-Mattila, 10727/2018).

2.4 ELISA

Total and NP-specific antibody levels were measured by ELISA on half-area 96-well plates (Greiner Bio-One, 675061). Wells were coated overnight at +4°C with capture antibodies (2 µg/mL) or NP-conjugated carrier proteins, $NP_{(1-9)}$-BSA or $NP_{(>20)}$-BSA (N-5050L, N-5050H, Biosearch Technologies) at 50 µg/mL in 25 µL PBS. Non-specific binding sites were blocked for 2 hours in 150 µL of blocking buffer (PBS, 1% BSA, 0.05% NaN_3). Appropriate, experimentally determined dilutions (see below) of 50 µL serum samples in blocking buffer were added for overnight incubation at +4°C. Biotin-conjugated detection antibodies (2 µg/mL) in 50 µL of blocking buffer were added for 1 hour followed by 50 µL ExtrAvidin-Alkaline phosphatase (E2636, Sigma-Aldrich, 1:5000 dilution) in blocking buffer for 1 hour at room temperature (RT). In between all incubation steps, plates were washed with 150 µL washing buffer (PBS, 0.05% Tween-20) either 3 times for the steps before sample addition or 6 times after addition of the mouse sera. The final wash was completed with 2 times wash with 150 µL of water. Finally, 50 µL of Alkaline phosphatase-substrate, SIGMAFAST p-Nitrophenyl phosphate, (N2770, Sigma-Aldrich) solution was added and OD was measured at 405 nm. Serum dilutions were determined experimentally to fall into linear part of the dose-response curve of the absorbance measurements for any given isotype and typical values are as follows: IgM levels (1:3000–1:4000), IgG levels (1:20000–1:80000). Different dilutions of AP-streptavidin were used where necessary. Typical time for AP-substrate incubation before measurement was about 30 min at RT.

All ELISA samples were run in duplicates, OD values were averaged and blank background was subtracted. Absolute concentrations of total antibody levels were extrapolated from calibration curves prepared by serial dilution of mouse IgM or subclasses of IgG from C57Bl/6 immunoglobulin panel. Relative NP-specific antibody levels were extrapolated from reference curves prepared by serial dilution of pooled serum, in which the highest dilution step received an arbitrary unit of 0.5.

2.5 Immunophenotyping

All cells were isolated in B cell isolation buffer (PBS, 2% FCS, 1 mM EDTA). Bone marrow cells were isolated by flushing the buffer through mouse femoral and tibial bones. Splenocytes were isolated by mashing the spleen in small buffer volumes with syringe plunger in 48-well plates. Peritoneal cavity cells were isolated by filling the cavity with ~10 mL buffer volume through puncture and collecting the fluid back. Cell suspensions were filtered through 70 µm nylon cell strainers. As a general flow cytometry protocol all following steps were done in flow cytometry buffer I (PBS, 1% BSA). Fc-block was done with 0.5 µL anti-mouse CD16/32 antibodies in 70 µL of flow cytometry buffer I for 10 min and cells were stained for 30 min. Washings were done 3 times in 150 µL of flow cytometry buffer I. All steps were carried out on ice in U-bottom 96-well plates at cell density of $0.25–0.5 \times 10^6$/well. Before acquisition, cells were resuspended in 130 µL flow cytometry buffer II (PBS, 2.5% FCS). Samples were acquired on BD LSR Fortessa, equipped with four laser lines (405 nm, 488 nm, 561 nm, 640 nm). Compensation matrix was calculated and applied to samples either in BD FACSDiva™ software (BD Biosciences) or in FlowJo (Tree Star, Inc) based on fluorescence of conjugated antibodies using compensation beads (01-1111-41, Thermo Fisher Scientific). FMO (fluorescence minus one) controls were used to assist gating. Data was analyzed with FlowJo software.

2.6 B cell isolation

Splenic B cells were Isolated with EasySep™ Mouse B Cell Isolation Kit (19854, Stem Cells Technologies) according to manufacturer's instructions and let to recover in RPMI (10% FCS,

178 20 mM HEPES, 50 μM β-mercaptoethanol, 1:200 Pen/Strep) in an incubator at +37°C and 5% CO_2 for
179 1-2 hours.
180
181 **2.7 Class-switch recombination and proliferation**
182 Isolated splenic B cells (~10–20×10^6 cells) were stained first with 5 μL (5mM) Cell Trace Violet
183 (C34557, Thermo Fisher Scientific) in 10 mL of PBS for 10 min at RT and let to recover in complete
184 RPMI (+37°C, 5% CO_2) for 1–2 hours. To induce class-switching, B cells were cultured on 24-well
185 plates at 0.5×10^6/mL density in complete RPMI supplemented with indicated doses of LPS (4 μg/mL),
186 CD40L (150 ng/mL), IL-4 (5 ng/mL), IFN-γ (100 ng/mL) and TGF-β (3 ng/mL) for 3 days. Cells were
187 blocked with anti-mouse anti-CD16/32 and stained for 30 min with antibodies against IgG subclasses.
188 Additionally, cells were stained with 4 μg/mL 7-AAD (ABD-17501, Biomol) for live/dead cell
189 discrimination and samples were acquired on BD LSR II equipped with 3 laser lines (405 nm, 488 nm,
190 640 nm) and analyzed with FlowJo software.
191
192 **2.8 B cell receptor signaling and immunoblotting**
193 For analysis of BCR signaling, isolated splenic B cells were starved for 10 min in plain RPMI and
194 0.5 × 10^6 cells in 100 μL of plain RPMI were stimulated in duplicates with anti-mouse IgM μ-chain-
195 specific (anti-IgM) antibodies either in solution or bound to the culture dish surface, for 3, 7 and 15 min.
196 For solution stimulation, 5 μg/mL of anti-IgM was used, in 96-well plates. For surface-bound mode, 48-
197 well plates were coated with 5 μg/mL of anti-IgM antibodies in 120 μL of PBS at +4°C, overnight, and
198 washed 3 times with 500 μL of ice-cold PBS before experiment. After activation, B cells were instantly
199 lysed with 25 μL of 5x SDS lysis buffer (final: 62.5 mM TrisHCl pH ~6.8, 2% SDS, 10% Glycerol,
200 100mM β-mercaptoethanol, bromphenol blue) and sonicated for 7.5 min (1.5 mL tubes, high power, 30 s
201 on/off cycle, Bioruptor plus, Diagenode). Lysates (20–30 μL) were run on 8–10% polyacrylamide gels
202 and transferred to PVDF membranes (Trans-Blot Turbo Transfer System, Bio-Rad). Membranes were
203 blocked with 5% BSA in TBS (TBS, pH ~7.4) for 1 hour and incubated with primary antibodies
204 (~1:1000) in 5% BSA in TBST (TBS, 0.05% Tween-20) at +4°C, overnight. Secondary antibody
205 incubations (1:20000) were done for 2 hours at RT in 5% milk in TBST for HRP-conjugated antibodies
206 and with addition of 0.01% SDS for fluorescently-conjugated antibodies. Washing steps were done in 10
207 mL of TBST for 5 × 5 min. Membranes were scanned with Odyssey CLx (LI-COR) or visualized with
208 Immobilon Western Chemiluminescent HRP Substrate (WBKLS0500, Millipore) and ChemiDoc MP
209 Imaging System (Bio-Rad). Phospho-antibodies were stripped in 25 mM Glycine-HCl buffer, pH ~2.5
210 for 10 min, membranes were blocked and probed again for evaluation of total protein levels. Images
211 were background subtracted and the raw integrated densities for each band were measured in ImageJ.
212 Ratios of phosphorylated-vs-total protein levels were analyzed with ratio paired t test. For data
213 presentation these ratios were normalized to WT value at 0 min.
214
215 **2.9 Intracellular Ca^{2+} flux**
216 Splenic B cells were resuspended at a concentration of 2.5-5 × 10^6 cell/mL in RPMI supplemented
217 with 20 mM HEPES and 2.5% FCS and loaded with 1 μM Fluo-4 (F14201, Thermo Fisher Scientific)
218 and 3 μM Fura Red (F3021, Thermo Fisher Scientific) for 45 min (+37°C, 5% CO_2). Cell suspension
219 was diluted in 10 volumes of complete RPMI and incubated for 10-15 min at RT. Cells were centrifuged
220 at 200 g, at RT for 5 min and resuspended at 2.5 × 10^6 cells/mL in PBS supplemented with 20 mM
221 HEPES, 5 mM glucose, 0.025% BSA, 1 mM $CaCl_2$, 0.25 mM sulfinpyrazone (S9509, Sigma-Aldrich),
222 2.5% FCS. Cells were allowed to rest at RT for 20 min and were kept on ice before acquisition. Anti-
223 IgM antibodies were added into prewarmed (+37°C, 5 min) B cell suspension aliquots to final
224 concentrations of 10, 5, 2.5 and 1 μg/mL and samples were acquired on BD LSR Fortessa. Alternatively,
225 equimolar concentrations of anti-IgM $F(ab')_2$ fragment were used. Fluorescence of Fluo-4 and Fura Red

were recorded by a continuous flow for 5 min. Data was analyzed in FlowJo and presented as ratiometric measurement of Fluo-4/Fura Red median intensity levels.

Peritoneal cavity B cells were washed in L-15 medium, resuspended in 75 µL acquisition buffer (HBS (HEPES buffered saline):L-15 (1:1 ratio), 2.5 µM probenecid (P8761, Sigma-Aldrich)) and labeled by addition of 75 µL acquisition buffer with 10 µM Fluo-4 for 5 min at +37°C. Cells were washed in 1 ml, resuspended in 200 µL and divided into two wells. B cells were prestained for 10 min on ice with anti-CD23-AF594 antibodies, washed and resuspended in 100 µL of acquisition buffer on ice. Samples were prewarmed (+37°C) in a total volume of 300 µL of acquisition buffer and 50 µL of anti-IgM $F(ab')_2$-AF633 were added. Cells were acquired on BD LSR Fortessa for 3-5 min and analyzed in FlowJo.

2.10 Scanning electron microscopy

For the analysis of resting B cells, wells of the microscopy slides (10028210, Thermo Fisher Scientific) were coated with CellTak (354240, Corning) in PBS (3.5 µg/cm^2 of surface area, according to manufacturer's recommendations) for 20 min (RT), washed once with water and allowed to dry. For the analysis of activated B cells, wells were coated with 5 µg/mL of anti-IgM in PBS for 1 h (RT) and washed in PBS. 10^5 B cells in 20 µL of complete RPMI were placed on coated wells for 10 min (+37°C, 5% CO_2) and fixed by adding 20 µL PFA in PBS (4% PFA final, pH 7.0–7.5) for 15 min. Samples were further fixed in 4% PFA/2.5% gluteraldehyde in PBS for 30 min, washed in PBS and post-fixed in 1% OsO_4 containing 1.5% potassium ferrocyanide, and dehydrated with a series of increasing ethanol concentrations (30%, 50%, 70%, 80%, 90%, 96% and twice 100%). Specimens were immersed in hexamethyldisilazane and left to dry by solvent evaporation. The cells were coated with carbon using Emscope TB 500 Temcarb carbon evaporator and imaged with Leo 1530 Gemini scanning electron microscope.

2.11 Immunofluorescence microscopy and cell spreading

TIRF microscopy. MatTek microscopy dishes were coated with 7.5 µg/mL of anti-IgM antibodies in PBS at +37°C for 30 min and washed once with PBS. Isolated splenic B cells (10^6) were left unstained or labeled with 0.17 µL of anti-B220-AF647 antibodies in 400 µL PBS for 10 min in 1.5 mL tubes on ice, spun (2500 rpm, 5 min), washed twice in 900 µL of ice-cold PBS and resuspended in 200 µL of Imaging buffer (PBS, 10% FBS, 5.5 mM D-glucose, 0.5 mM $CaCl_2$, 0.2 mM $MgCl_2$). Equal amounts of unstained and labeled cells of different genotypes were mixed and loaded onto coated MatTek dishes at 35 µL/well. Cells were incubated for 10 min (+37°C, 5% CO_2), fixed in pre-warmed (+37°C) 4% formaldehyde/PBS for 10 min (RT), permeabilized in 0.1% Triton X-100/PBS for 5 min (RT), washed once with PBS and blocked in blocking buffer (PBS, 1% BSA) at +4°C (overnight). Cells were stained with 1:50 Phalloidin-AF555 and 1:500 anti-pTyr primary antibody (4G10) in blocking buffer for 1 hr (RT), washed 4 times with PBS, and stained with 1:500 secondary anti-mouse IgG2b-AF488 in blocking buffer for 1 hr (RT), washed 4 times in PBS and imaged in PBS with total internal reflection fluorescence (TIRF) mode in DeltaVision OMX Imaging System (GE Healthcare). TIRF images of cortical actin and pTyr were processed with ImageJ macro using B220 and bright-field channels to discriminate between attached WT or MIM-KO cells. Spreading area (determined on pTyr channel), mean fluorescence intensity and total fluorescence intensity (integrated density) of phalloidin and pTyr staining of each cell were analyzed (~50–340 cells per sample). For cumulative scatter plots, equal numbers (here 92 cells) were randomly selected from each experiment.

Spinning disk confocal microscopy. 12-well PTFE diagnostic slides (Thermo Fisher Scientific, #10028210) were coated with 5 µg/mL anti-mouse IgM (µ-chain-specific antibodies) in PBS at +4°C O/N and washed with PBS. As a non-activated control, wells were coated with 4 µg/mL fibronectin. Isolated splenic B cells (10^6/ml) were labeled with 1µM CFSE (21888, Sigma-Aldrich) or left unlabeled. Equal amounts of unstained and labeled cells of different genotypes were mixed (1:1 ratio) and seeded at density of 100.000 cells/well. Dye-switched experiments were performed systematically. Cells were

276 incubated for 3, 5, 7, 10 or 15 min (+37°C, 5% CO_2), fixed in 4% formaldehyde/PBS for 10 min (RT)
277 and permeabilized/blocked in 0.3% Triton X-100/5% donkey serum/PBS for 20 min (RT). Staining was
278 performed in 0.3% Triton X-100/1% BSA/PBS at +4°C O/N, followed by washes with PBS and
279 incubation with the secondary antibodies for 30 min at room temperature in PBS. Samples were
280 mounted in FluoroMount-G (Thermo Fisher Scientific). Images were acquired on 3i CSU-W1
281 (Intelligent Imaging Innovations) Marianas spinning disk confocal microscope equipped with 63x Zeiss
282 Plan-Apochromat objective and a Photometrics Prime BSI sCMOS camera. Cells were visualized at the
283 plane of contact and 5-10 fields of view per sample were acquired. Images of F-actin, pBtk and pSyk
284 were processed with ImageJ using CTV channel to discriminate between WT or MIM-KO cells.
285 Spreading area (determined on the phalloidin channel) and mean fluorescence intensity of pBtk or pSyk
286 staining per cell were analyzed (~25–150 cells per condition per experiment).
287
288 **2.12 Supported lipid bilayers**
289 Artificial planar lipid bilayers containing GPI-linked mouse ICAM-1 (200 molecules/μm^2) were
290 formed as previously described (Grakoui et al., 1999; Carrasco et al., 2004). Briefly, unlabeled GPI-
291 linked ICAM-1 liposomes and liposomes containing biotinylated lipids were mixed with 1,2-dioleoyl-
292 PC (DOPC) (850375P, Avanti lipids, Inc) at various ratios to obtain specified molecular densities.
293 Planar membranes were assembled on FCS2 dosed chambers (Bioptechs) and blocked with PBS/2%
294 FCS for 1 h at RT. Antigen was tethered by incubating membranes with AF647-streptavidin, followed
295 by monobiotinylated anti-kappa light chain antibodies (20 molecules/μm^2). The isolated B cells from
296 WT and $MIM^{-/-}$ mice were labeled with 1µM CFSE (21888, Sigma-Aldrich) or left unlabeled, mixed at
297 1:1 ratio, and injected into prewarmed chambers (4×10^6 cells/chamber, +37°C) with 100 nM
298 recombinant murine CXCL13. Fluorescence, differential interference contrast (DIC), and interference
299 reflection microscopy (IRM) images were acquired at the plane of the cell contact in one position once
300 every 30 s immediately after injecting the cells into the chamber for 10 min. After the 10 min movie was
301 acquired, several snapshots were acquired for quantification of the mature synapses in different locations
302 of the chamber at 10-15 min after cell injection. All assays were performed in PBS, supplemented with
303 0.5% FCS, 0.5 g/L D-glucose, 2 mM MgCl and 0.5 mM $CaCl_2$. Images were acquired on Zeiss Axiovert
304 LSM 510-META inverted microscope, equipped with 40x oil-immersion objective (Madrid), or Zeiss
305 LSM 780 inverted microscope, equipped with 40x water-immersion objective (Turku), and analyzed by
306 ImageJ. The spreading area (determined on IRM channel), area of collected antigen and mean
307 fluorescence intensity of antigen were quantified from each experiment (~100 cells per experiment).
308
309 **2.13 Intracellular Ca^{2+} flux on supported lipid bilayers**
310 Splenic WT or $MIM^{-/-}$ B cells (3.2×10^6) were resuspended in 75 µL of L-15 medium and labeled
311 by addition of 75 µL of HBS (HEPES buffered saline), supplemented with 2.5 µM probenecid and 20
312 µM Fluo4 for 5 minutes at +37°C. Cells were washed in 1 mL HBS-probenecid and resuspended in 500
313 µL HBS-probenecid for immediate injection into FCS2 chambers. Acquired movies were preprocessed
314 with ImageJ and analyzed with a MATLAB implemented high-throughput software *CalQuo*[2] (Lee et al.,
315 2017). Cells were categorized as single peak, oscillatory or not triggering. Cells showing more than two
316 intensity peaks are classified as oscillatory. Data presented as mean percentages of 3 independent
317 experiments with at least 1000 cells analyzed per experiment.
318
319 **2.14 Metabolic assay**
320 Splenic B cells were seeded at a density of 10^6 cells/mL in complete RPMI and treated with
321 indicated combinations of IL-4 (10 ng/mL), anti-mouse IgM (10 µg/mL), LPS (4 µg/mL) and CpG
322 (10 µg/mL) for 24 h at +37°C, 5% CO_2 in a humidified incubator. Cells were then spun and resuspended
323 in Seahorse XF RPMI (103576-100, Agilent), supplemented with 1 mM pyruvate, 2 mM L-glutamine
324 and 10 mM D-glucose. Cell number was adjusted and 0.15×10^6 cells were seeded per well on a 96-well
325 XF plate, pre-coated with CellTak (354240, Corning). Plate coating was done with 22.4 µg/mL CellTak

326 in $NaHCO_3$, pH 8.0 at +4°C overnight, followed by two washings with water. Seeded cells were spun at
327 200 g for 1 min with no break and left for 1 h at 37°C to attach to coated wells in a humidified incubator
328 without CO_2 to avoid medium acidification. Seahorse XF96 plate (101085-004, Agilent) was used
329 following the manufacturer's instructions for XF Cell Mito Stress Test Kit (103015-100, Agilent). In
330 this test, sequentially, 1 μM oligomycin, 2 μM FCCP and 0.5 μM rotenone / antimycin A were added to
331 the media. Oxygen consumption rate (OCR) and extracellular acidification rate (ECAR) data were
332 recorded by WAVE software (Agilent). OCR and ECAR data were normalized to cell count and first
333 baseline measurement of WT cells. Basal, maximum and spare respiratory capacities were extracted
334 with area under curve analysis in GraphPad Prism.
335

336 **2.15 Analysis of mitochondria**

337 For TMRE staining, B cells were washed in 150 μL PBS, stained with 1:500 Zombie Violet for
338 dead cell discrimination in PBS on ice, washed 2 × 100μL with complete RPMI and stained with
339 5 nM TMRE (T669, Thermo Fisher Scientific) in 200 μL complete RPMI at RT for 20 min.
340 Resuspended in 150 μL of complete RPMI, cells were immediately analyzed by flow cytometry, on BD
341 LSR Fortessa.
342 For Tom20 staining, B cells were stained with Zombie Violet as described above, fixed with 1.6%
343 formaldehyde in PBS for 10 min, washed 2 × 150 μL PBS, permeabilized with 0.5% Triton X-100 in
344 PBS for 5 min at RT, blocked for 1 h at RT. Incubation with primary Tom20 antibodies was done at
345 1:500 dilution for 30 min, followed by 3 × 150 μL washes, staining with 1:1000 dilution of anti-rabbit-
346 AF488 secondary antibodies, and 3 × 150 μL washes. Cells were then resuspended in 130 μL and
347 analyzed by flow cytometry, on BD LSR Fortessa. Antibody incubations, blocking and washings were
348 done in flow cytometry buffer I on ice. Geometric mean fluorescence intensities were extracted with
349 FlowJo software.
350

351 **2.16 Statistics and data presentation**

352 Statistical analysis was performed in GraphPad Prism. Student's t test was applied to the data
353 comparing WT and MIM-KO groups. Antibody titres and microscopy data were analyzed with unpaired
354 two-tailed t test unless otherwise stated. Additionally, for TIRF microscopy datasets, geometric means
355 were extracted for each biological replicate and means were analyzed by ratio paired t test. In other
356 experiments, ratio paired t test was also applied when pairing WT and MIM-KO data was based on the
357 day of the experiment as indicated in figure legends. Multiple measures two-way ANOVA was
358 additionally used to compare the antibody responses upon immunization. Data presented as Mean ±
359 SEM, unless stated otherwise. Significance is denoted as * $p<0.05$, ** $p< 0.01$, *** $p< 0.001$, ****
360 $p<0.0001$. Inkscape and Adobe Illustrator were used for figure assembly, and Biorender for schematics.
361

362 **3 Results**

363 **3.1 Largely normal B cell development and maturation of B cells in MIM$^{-/-}$ mice**

364 Mice with targeted disruption of *Mtss1* gene (MIM$^{-/-}$), lacking the expression of MIM, were
365 generated previously (Saarikangas et al., 2011). Splenic B cells, that normally show robust MIM
366 staining in immunoblot, isolated from these mice showed no detectable MIM expression (Fig. 1A). To
367 investigate the possible functions of MIM in the B cell compartments, we first examined the B cells in
368 the bone marrow. We notified a slightly increased number of hematopoietic progenitors, as defined by
369 CD117^{+} CD19^{-} cells but found no apparent differences in the numbers of CD19^{+} and CD19^{+} IgM^{+}
370 populations between age-matched wild type (WT) and MIM$^{-/-}$ mice (Fig. 1B-C, Suppl. Fig. S1B). We
371 then carried out more detailed analysis of the bone marrow B cells with additional surface markers to
372 resolve consecutive developmental stages from common lymphoid progenitors to immature and mature
373 recirculating B cells (gating strategy shown in Suppl. Fig. S1A). We found no significant differences
374 between WT and MIM$^{-/-}$ mice in any of these developmental stages (Fig. 1D).
375
376 Next, we went on to analyze the maturation of B cells and their different subsets in the periphery
377 (gating strategy shown in Suppl. Fig. S2A, B). No defects were observed in the overall percentages of
378 CD19^{+} B cells or major T cell subsets in the spleen (Fig. 1E). Also the proportions of transitional (T1–3)
379 and follicular (Fo) cells were not significantly altered, while marginal zone (MZ) B cells appeared
380 slightly elevated (Fig. 1F). A special self-renewing population of B cells concentrate in the peritoneal
381 and pleural cavities. To analyze these B1 cells, we isolated cells from the peritoneal cavity of MIM$^{-/-}$ and
382 WT mice. We found no significant differences in the proportions of CD5^{+} (B1a), CD5^{-} (B1b) or mature
383 peritoneal B cells (B2) (Fig. 1G). These results demonstrate that the development of different B cell
384 subsets, both in the bone marrow as well as in the periphery, does not depend on MIM.
385

386 **3.2 MIM$^{-/-}$ B cells are defected in BCR signaling upon activation with surface-bound antigens**

387 Previous cell biological studies in other cell types, supported by various biochemical assays, have
388 proposed a role for MIM at the interface of the plasma membrane and the actin cytoskeleton (Lee et al.,
389 2007; Lin et al., 2005; Mattila et al., 2003, 2007; Saarikangas et al., 2011, 2015). The actin cytoskeleton
390 is intimately involved in the activation of B cells on antigen presenting cells by enabling the spreading
391 of the cells and the formation of the immunological synapse (Harwood and Batista, 2010). Interestingly,
392 the organization of the plasma membrane and the actin cytoskeleton have also been shown to regulate
393 the signaling capacity of the BCR (Treanor et al., 2010; Mattila et al., 2013, 2016). To examine the role
394 of MIM in BCR signaling, we, first, analyzed the mobilization of intracellular calcium, one of the most
395 dramatic immediate consequences of BCR triggering. We isolated splenic B cells from WT and MIM$^{-/-}$
396 mice, loaded them with Fluo-4 and Fura Red, and stimulated with decreasing concentrations of surrogate
397 antigen, either full antibodies against mouse IgM BCR (anti-IgM), or their F(ab')$_2$ fragments, while
398 analyzing the response by flow cytometry. Ratiometric analysis of Fluo-4/Fura Red fluorescence
399 intensities revealed similar elevation of intracellular Ca^{2+} levels in both WT and MIM$^{-/-}$ B cells (Fig. 2A,
400 Supplementary Fig S3F). We also analyzed the calcium response in peritoneal cavity B cells, which
401 were loaded with Fluo-4, prestained with CD23-Alexa Fluor (AF)-594 just before acquisition and
402 stimulated with AF633-labeled anti-IgM antibodies, allowing distinction between B1 (IgM^{+} CD23^{-}) and
403 B2 (IgM^{+} CD23^{+}) cells. Intracellular Ca^{2+} mobilization was found comparable between WT and MIM$^{-/-}$
404 cells also in these two B cell subsets (Suppl. Fig. S3A).
405
406 To study the BCR signaling in more detail, we next analyzed activation of individual components of
407 BCR signaling pathway by looking at phosphorylation levels of downstream effector molecules. Splenic
408 B cells were stimulated with soluble or surface-bound anti-IgM antibodies for 3, 7 and 15 min and
409 analyzed by immunoblotting. As expected, both stimulatory conditions induced rapid activation of BCR
410 signaling components, as detected by the levels of phosphorylated signaling proteins. Importantly,

411 MIM$^{-/-}$ B cells showed clear defects in signaling in response to surface-bound anti-IgM. Most of the
412 analyzed molecules, including Syk, CD19, Btk, p65 NF-κB and MAPK1/2 showed significant reduction
413 in their activation (Fig 2B, C). Consistently, we found similar differences when using either 5 or
414 1 μg/ml of surface-tethered anti-IgM, or corresponding amounts of $F(ab')_2$ fractions of anti-IgM
415 (Suppl. Fig. S3D-E). The signaling components studied can be classified into different cascades from the
416 proximal players to downstream effectors. While MIM$^{-/-}$ cells showed robust defects in proximal
417 signaling molecules, the extent to which they affected the downstream cascades alternated. The defects
418 in PI3K pathway were largely recovered at the level of Akt. At the same time, the levels of pp65 NF-κB
419 and pMAPK1/2 were decreased, suggesting that MIM$^{-/-}$ B cells were inefficient in triggering the
420 diacylglycerol (DAG)-PKC module, targets of which both NF-κB and MAPK1/2 are (Mérida et al.,
421 2010). Interestingly, when we studied activation of BCR by soluble ligand, anti-IgM surrogate
422 antibodies in solution, MIM$^{-/-}$ B cells only showed significant defects in the activation of the proximal
423 kinase Syk, but normal activation of other signaling components (Suppl. Fig S3B, C). These results
424 place MIM as a regulator of, specifically, BCR signaling by surface-bound antigen, function that clearly
425 depends on the fine-tuned activities of the actin cytoskeleton (Bolger-Munro et al., 2019) and could fit
426 well with the previously postulated role of MIM as an organizer of the actin cytoskeleton-membrane
427 interface.
428

429 **3.3 The morphology and formation of the immunological synapse is unaltered in MIM$^{-/-}$ B cells**

430 The actin cytoskeleton is one of the major organizers of cell shape. To explore whether MIM$^{-/-}$ B
431 cells showed any changes in the overall morphology, we visualized them using scanning electron
432 microscopy (SEM), either in resting state or after 10 min activation by surface-tethered anti-IgM,
433 mimicking the formation of the immunological synapse. In SEM, the morphology of MIM$^{-/-}$ B cells
434 appeared grossly similar to WT cells (Fig. 3A). However, to perform another, more quantitative
435 analysis, we turned to fluorescent microscopy. We activated B cells on anti-IgM-coated coverslips and
436 analyzed the area of spreading using total internal reflection fluorescence (TIRF) microscopy, an
437 imaging method ideal for visualization of the cell membrane-coverslip interface. The analysis of the
438 TIRF images revealed that MIM$^{-/-}$ B cells spread slightly but consistently less than their WT counterparts
439 (Fig. 3B). To measure overall phosphorylation at the contact region, we stained the cells with anti-
440 phospho-Tyrosine (pTyr) antibodies. Mean fluorescence intensities of pTyr were also reduced in MIM$^{-/-}$
441 B cells. To investigate the impaired BCR signaling and its kinetics in more details, we next activated the
442 B cells on anti-IgM coated coverslips for different timepoints and stained them with anti-pBtk and anti-
443 pSyk antibodies, as well as phalloidin. Quantification of the pBtk and pSyk in the contact plane showed
444 significantly reduced levels of these signals, as well as levels of spreading, in MIM$^{-/-}$ cells through
445 different time points (Fig 3C). The diminished area of spreading and kinase signaling detected by
446 microscopy are well in line with our results from immunoblotting that also showed impaired BCR
447 signaling. However, based on the SEM data and F-actin staining of the splenocytes, MIM$^{-/-}$ cells do not
448 exhibit major morphological defects in their actin cytoskeleton (Fig. 3A–C).
449

450 Recognition of surface-bound antigens *in vivo* can involve interaction of B cells with antigenic
451 determinants on substrates of various physical properties. While stiff substrates can include bacterial cell
452 wall components or extracellular matrix-linked antigens, perhaps more typical encounter occurs on the
453 surface of antigen presenting cells, where antigens remain laterally mobile. To understand if MIM$^{-/-}$ B
454 cells can initiate robust BCR signaling upon encounter with mobile antigens, we first settled Fluo-4-
455 loaded WT and MIM$^{-/-}$ B cells on AF555-labeled supported lipid bilayers (SLB), containing anti-kappa
456 antibodies and ICAM-1. Mobilization of Ca^{2+} was imaged for 5 min by spinning disk confocal
457 microscopy and analyzed with the *CalQuo*^{2} software package for MATLAB (Lee et al., 2017). Analysis
458 of median Fluo-4 intensity and proportions of MIM$^{-/-}$ B cells with single peak or oscillatory Ca^{2+}
459 intensity profiles revealed no differences between MIM-KO and WT cells (Fig. 3D). Next, we evaluated
460 the ability of MIM-KO cells to spread and form immunological synapses on SLBs. We performed live-

461 cell imaging of WT and MIM-KO cells and recorded interference reflection microscopy (IRM) images
462 to detect the overall contact area of the cells, and fluorescent antigen signal to follow antigen gathering
463 in the synapse (Fig. 3E). The movies showed fast cell spreading, reaching maximum in 1-2 minutes,
464 followed by slower contraction response coinciding with antigen accumulation to form the mature
465 immunological synapse. We did not detect any differences in the kinetics of synapse formation in MIM-
466 KO cells as compared to WT counterparts. Also, in the mature synapses, analyzed after 10 minutes of
467 contact with the SLB, MIM$^{-/-}$ B cells accumulated normal amounts of antigen in the center of the
468 synapse (Fig. 3E). Thus, while MIM modulates BCR signaling and spreading responses upon antigen
469 contact on stiff substrates, upon engagement of membrane-bound mobile antigens the cells are able to
470 engage and gather normal amounts on antigen to the center of the immunological synapse. On
471 membranous surfaces, spreading and contraction response is complemented with dynamic fluctuations
472 of F-actin-rich protrusions, making the regulation of the cytoskeletal structures distinct from spreading
473 on immobilized-antigens.
474
475 **3.4 MIM is required for an efficient antibody response against T-independent antigen**
476 To test if the defected signaling in MIM$^{-/-}$ B cells leads into problems in mounting of the immune
477 responses, we went on to examine antibody levels of our mice first at the basal state and then upon
478 immunization with T cell-independent (TI) or T cell-dependent (TD) model antigens. We saw no
479 significant changes in the basal antibody levels in the sera of WT and MIM$^{-/-}$ mice (Fig. 4A). To study
480 the development of antibody responses towards TI antigens, we immunized mice with NP-FICOLL
481 (Fig. 4B–D). Throughout the examination time course of 28 days, we found reduced levels of both total
482 and NP-specific IgM in MIM$^{-/-}$ mice (Fig. 4C). Interestingly, we also detected impaired responses in the
483 total levels of IgG subtypes, most profound in IgG2b, while the production of NP-specific IgG
484 subclasses was not impaired (Fig. 4D).
485
486 For immunizations with TD protein antigen, we used NP-KLH in alum and followed up the primary
487 response for four weeks. Four months later, we stimulated a memory response and followed that for 2
488 weeks (Suppl. Fig. S4A). In contrast to TI immunization scheme, we found that MIM$^{-/-}$ mice were as
489 efficient in mounting antibody responses to a protein antigen as their WT counterparts (Suppl. Fig. S4B-
490 C). Analysis of the memory responses also showed equal levels of NP-specific IgG for all subclasses
491 (Suppl. Fig. S3D). Furthermore, we analyzed affinity maturation by comparing binding to low and high
492 densities of NP-epitopes in ELISA, and found no significant differences between WT and MIM$^{-/-}$ mice
493 (Suppl. Fig. S4E).
494
495 In the light of defects in BCR signaling and TI immune responses in MIM$^{-/-}$ mice, normal antigen-
496 specific IgG immune responses may point towards compensation by other signals in the system, such as
497 T cell help. To dissect the B cell intrinsic features linked to IgG antibody responses in more detail, we
498 set up an *in vitro* assay for class-switch recombination (CSR). We provoked B cells to change the
499 isotype of the produced Ig molecules, by mimicking cellular events of pathogen encounter or T cell help
500 during maturation of IgG antibody responses. As expected, 3 days of B cells activation with LPS or
501 CD40L in combination with cytokines induced switching of surface-expressed Ig molecules to different
502 IgG isotypes, as detected by flow cytometry. Consistent with the *in vivo* data on generation of NP-
503 specific IgG antibody responses, MIM$^{-/-}$ B cells switched normally in all tested conditions, producing
504 similar percentages of IgG^{+} cells, indicating that MIM is not required for CSR in response to TLR
505 ligands or CD40L and cytokines. In fact, switching rates into the most common isotypes were even
506 slightly higher for MIM$^{-/-}$ B cells when stimulated with LPS (Suppl. Fig. S5A–D). We also loaded the
507 cells with Cell Trace Violet dye, which allowed us to analyze fluorescence profiles of dividing splenic B
508 cells in response to these stimuli. We found robust proliferation of MIM$^{-/-}$ B cells when they were
509 activated with LPS, CD40L or anti-IgM + CD40L (Suppl. Fig. S5E). Analysis of the proliferation
510 indices (PI) showed close to equal proliferation of MIM-KO and WT cells in all conditions tested.

511 Notably, the division indices (DI) of MIM$^{-/-}$ B cells were moderately, but significantly, increased in
512 CD40L + IFNg cultures, reflecting smaller numbers of cells left undivided, further indicating normal or
513 even improved ability of MIM$^{-/-}$ cells to react to conditions similar to T cell help.
514
515 Our immunization studies suggest that MIM plays a role in IgM antibody responses to TI type 2
516 antigens, which haptenated FICOLL represents. However, MIM is dispensable for the development of
517 antibodies against TD protein antigens. The ability to switch the antibody class upon polyclonal
518 activation with LPS, TI type 1 antigen, appeared normal. Although by using a conventional MIM
519 knockout mouse model we cannot rule out the influence of other immune and stromal cells on the
520 immune responses generated *in vivo*, IgM antibody responses to TI antigens are considered to be largely
521 B cell intrinsic and in case of TI type 2 antigens rely primarily on intact BCR signaling. Thus, the
522 defects in IgM antibody responses are in line with the diminished BCR signaling observed *in vitro*
523 (Fig. 2B–C; Fig 3B–C).
524
525 **3.5 MIM$^{-/-}$ B cells show higher metabolic profile upon LPS and CpG stimulation**
526 Our results suggest that MIM plays a role in antibody responses to TI-2 antigens. *In vivo*, however,
527 T cell-independent antigens are usually associated with pathogenic determinants recognized by Toll-like
528 receptors, important modulators of B cell immune responses (Bekeredjian-Ding and Jego, 2009).
529 Activation of resting lymphocytes upon BCR engagement or recognition of microbial components
530 triggers dramatic changes in their metabolism. Upregulated metabolic activity meets the increased
531 energetic demands of activated cells and supports active proliferation and differentiation into antibody-
532 secreting cells. We next analyzed the metabolic reprogramming potential of MIM$^{-/-}$ B cells upon
533 activation via either BCR or TLRs, or combination of both. The rates of cellular oxygen consumption
534 (oxygen consumption rate, OCR), an estimate of mitochondrial respiration, and extracellular
535 acidification (extracellular acidification rate, ECAR), an estimate of glycolysis, were measured with a
536 Mito Stress test in the Seahorse platform. In this assay, serial injections of oligomycin, Carbonyl
537 cyanide-4-(trifluoromethoxy)phenylhydrazone (FCCP) and rotenone/antimycin A (Rot/AA) mixture,
538 sequentially inhibit ATP production, collapse the proton gradient membrane potential and finally shut
539 down mitochondrial respiration. This system allows measurement of the basal OCR, maximal and spare
540 respiratory capacities, as well as determination of non-mitochondrial respiration.
541
542 First, we analyzed metabolic responses to individual stimulations with BCR ligands or TLR
543 agonists. To this end, we activated WT and MIM$^{-/-}$ B cells with LPS, CpG or anti-IgM + IL-4 for 24 h
544 or kept them largely resting with IL-4 alone (Fig. 5A). Already samples treated with IL-4 alone showed
545 a slight but significant increase in the maximal respiration in MIM$^{-/-}$ B cells. Notably, we observed a
546 significant increase in the metabolic profile of MIM$^{-/-}$ cells as compared to WT counterparts upon
547 activation with TLR4 and TLR9 ligands, LPS or CpG. Approximately 20% increase in the maximum
548 respiration of MIM$^{-/-}$ cells was measured upon treatment with LPS or CpG. MIM$^{-/-}$ cells also showed
549 similar increase in the basal OCR levels and almost two-fold upregulation for spare respiratory capacity
550 upon CpG activation. In contrast to TLR stimulations, 24 h activation via BCR led to a slight diminution
551 in basal respiration and no differences in maximum and spare respiration levels in MIM$^{-/-}$ cells. The
552 preferred route of ATP generation, reflected by basal OCR to ECAR ratio, remained relatively constant
553 across conditions, indicating no major shifts in the balance of oxidative phosphorylation and glycolytic
554 metabolism.
555
556 To gain more understanding into the relationship of BCR and TLR signals in the activation of
557 MIM$^{-/-}$ cells, we then asked how the metabolic reprogramming is affected by simultaneous engagement
558 of BCR and TLR. To this end, we cultured WT and MIM$^{-/-}$ B cells for 24 hrs with combination of anti-
559 IgM + LPS or anti-IgM + CpG and analyzed their metabolic profiles (Fig. 5A). Surprisingly, we found
560 that TLR-mediated increase in oxidative metabolism in MIM$^{-/-}$ cells was restored to WT levels by

561 simultaneous BCR engagement. To more directly compare this data to anti-IgM-stimulated cells, where
562 IL-4 was added to increase survival of the cells, we carried out analysis of anti-IgM + LPS/CpG -
563 stimulated cells also in the presence of IL-4. We found that simultaneous engagement of BCR also in
564 these conditions reverted the TLR-mediated increase in oxidative metabolism in MIM$^{-/-}$ B cells closer to
565 WT levels (Suppl. Fig. S6A). However, the negative effect of anti-IgM was less efficient in presence of
566 IL-4, consistent with the finding that IL-4 supports metabolic reprograming towads higher oxidative
567 state levels in MIM$^{-/-}$ cells .
568
569 Finally, we asked if the higher metabolic activity of MIM$^{-/-}$ B cells reflects a *bona fide* change in the
570 mitochondrial activity or is a result of elevated mitochondrial biogenesis upon TLR-mediated metabolic
571 reprograming. To this end, we stained mitochondria with TMRE and antibodies against Tom20 to assess
572 mitochondrial membrane potential and mitochondrial mass, respectively. In freshly isolated splenic
573 MIM$^{-/-}$ B cells, we found slightly but significantly elevated mitochondrial mass without significant
574 increase in mitochondrial membrane potential (Fig. 5B). As expected, activation of B cells with either
575 anti-IgM + IL-4, LPS or CpG increased mitochondrial biogenesis and membrane potential, with CpG
576 inducing most potent response (Fig. 5C). However, WT and MIM$^{-/-}$ B cells showed comparable levels of
577 mitochondrial membrane potential as well as mitochondrial mass after TLR stimulation. This suggests
578 that the changes we observed in the metabolic activity of MIM$^{-/-}$ cells occur without detectable
579 additional mitochondrial biogenesis but are rather a function of increased efficiency that might not be
580 adequately represented by TMRE. Functional changes in the mitochondrial, and metabolic, activity may
581 also be reflected by cell size (Miettinen and Björklund, 2017). We found that CpG- but not LPS- or anti-
582 IgM + IL-4-activated MIM$^{-/-}$ cells often showed slightly increased forward scatter characteristics when
583 analyzed by flow cytometry (Suppl. Fig. S6B). Together, our results suggest that in response to TLR4,
584 TLR9 or IL-4 stimulation, MIM negatively regulates metabolic reprograming of B cells, decreasing
585 reserves of oxidative metabolism, which are accompanied by functional changes in the mitochondrial
586 activity, rather than mitochondrial biogenesis. Interestingly, in MIM$^{-/-}$ B cells, simultaneous engagement
587 of BCR reverts TLR-mediated increase in oxidative mitochondrial activity.
588

589 **4 Discussion**

590 In this study, we examined the enigmatic cytoskeleton-membrane linker protein MIM in B cells,
591 where it is strongly expressed and also implicated in B cell lymphomas (Yu et al., 2012). In our mouse
592 model, we found diminished TI antibody responses, as well as defected BCR signaling, indicative of a
593 role in B cell activation and mounting of humoral immune responses. Together with the upregulated
594 metabolic boost and normal proliferative responses in MIM$^{-/-}$ B cells upon TLR activation, our data
595 suggest a complex role for MIM in modulation of different signaling pathways and cell fitness.
596 The predisposition of another MIM knockout mouse strain to lymphomagenesis, reported by Zhan
597 and colleagues, is intriguing (Yu et al., 2012). We found the spleens of MIM$^{-/-}$ mice at the age of 2-7
598 months normal in size and cellularity, but as we did not perform aging experiments, we cannot preclude
599 problems later in life. Regarding B cell development, Zhan and colleagues at first showed aberrant levels
600 of total CD19^{+} or CD19^{+} IgM^{+} cells in lymphoid organs (Yu et al., 2012), yet later reported normal B
601 cell numbers (Zhan et al., 2016). Following the same gating strategy, the numbers of pre-B cells in our
602 MIM$^{-/-}$ strain appeared normal (Suppl. Fig. S1B–C), and we postulate that the observed discrepancies
603 may arise from differences in strain maintenance or mouse age at the time of immunophenotyping. The
604 possible consequences of the deletion of MIM for B cell development might also be too subtle to
605 manifest in all models. In our model, we however, noted mildly elevated numbers of MZ B cells in the
606 spleens of MIM$^{-/-}$ mice (Fig. 1F). The mouse strain generated by Zhan and colleagues used embryonic
607 stem (ES) cells with insertion of gene trap sequence between exons 3 and 4 (clone CSC156,
608 BayGenomics) (Yu et al., 2011). Notably, an independent attempt to recapitulate the generation of
609 MIM$^{-/-}$ strain with the same clone of ES cells resulted in an inefficient use of delivered splicing acceptor
610 site (Fahrenkamp et al., 2017). This left a considerable expression of full-length Mtss1 both at mRNA

611 and protein levels, and varible remaining expression levels between animals, indicative of lability of the
612 splicing. Lack of MIM expression in analyzed cells was, however, shown by Zhan and colleagues (Yu et
613 al., 2011, 2012). In our strain, where a neomycin cassette with several stop codons is inserted in exon 1
614 of *Mtss1*, low levels of alternative splicing have been previously observed. However, the generated
615 transcript translates into a N-terminally truncated polypeptide chain, where the critical I-BAR domain is
616 functionally inhibited, and which did not yield detectable levels of protein expression (Saarikangas et al.,
617 2011). In this study, confirmative of the lack of MIM expression in B cells, we also confirmed a clear
618 and repeatable loss of detectable protein expression in our substrain, using two different commercial
619 antibodies (Fig. 1A).
620
621 MIM$^{-/-}$ B cells exhibited consistently diminished phosphorylation of several BCR effector
622 molecules upon stimulation of BCR with surface-bound antigen (Fig. 2B, C). This defect was in line
623 with smaller area of spreading and reduced overall tyrosine phosphorylation detected by microscopy at
624 the site of contact with antigen (Fig. 3B–C). Although lower amount of engaged antigen due to
625 inefficient actin-dependent spreading response may partially contribute to the signaling defects observed
626 in MIM$^{-/-}$ B cells, defected BCR signaling also leads to diminished spreading, generating a feedback
627 loop. Signaling upon soluble antigen stimulation, on the other hand, was mostly normal showing only
628 slight diminution in the levels of pSyk (Suppl. Fig. S3B–C). This suggests that MIM participates in the
629 ability of B cells to discriminate between different types of antigens by playing a specific role in B cell
630 activation on surfaces. Although the differential responses of B cells to different forms of antigen are
631 nowadays widely accepted (Mattila et al., 2016; Snapper, 2018; Bolger-Munro et al., 2019), to our
632 knowledge there are only few molecules, such as CD19 and CD81 (Depoil et al., 2008; Mattila et al.,
633 2013), that have been reported to specifically regulate stimulation by surface-linked antigens with
634 mechanisms likely separate from structural roles in cell adhesion or spreading. We also found that while
635 stimulation with surface-bound antigen resulted to a certain degree in reduced phosphorylation of all the
636 tested BCR effectors, the defects in proximal BCR signaling, exemplified by reduced pSyk and pCD19,
637 did not propagate evenly downstream. Reduced pCD19 seemed to largely spare PI3K pathway (Otero et
638 al., 2001) as pAkt levels are on par with those of WT (Fig. 2B, C). At the same time, levels of both pNF-
639 κB and pMAPK1/2 were significantly reduced, suggesting defected DAG-PKC signaling module (Su et
640 al., 2002; Coughlin et al., 2005; Mérida et al., 2010). PKC-FAK axis has been implicated in the
641 regulation of force-dependent B cell activation (Shaheen et al., 2017), and could be involved in the
642 specific defects in response to surface-bound antigens that we observed. Regarding the previously
643 suggested role for MIM in DLBCL (Yu et al., 2012), it is worth noting that dysregulated BCR signaling
644 also plays a role in lymphomagenesis (Young and Staudt, 2013).
645
646 Our experiments on supported lipid bilayers (SLB) suggested that MIM$^{-/-}$ B cells are able to form
647 signaling-competent BCR-antigen microclusters and gather normal amounts of antigen in the center of
648 the immunological synapse (Fig. 3E). Therefore, in this model system, coupling of BCR to actin and
649 microtubule cytoskeleton, required for the cell spreading and antigen gathering, respectively, is not
650 notably defected (Schnyder et al., 2011; Liu et al., 2012). However, results from the laterally fluid SLBs,
651 cannot be directly compared to B cell stimulation by immobilized antigens. SLBs are also not fully
652 comparable to situations where the cells need to overcome frictional coupling of antigen-presenting
653 molecules to the membrane skeleton of the APC (Ketchum et al., 2014; Luxembourg et al., 1998;
654 Dillard et al., 2014). In addition, SLBs in our experiments were functionalized with ICAM-1, which is
655 known to lower the threshold for B cell activation (Carrasco et al., 2004).
656
657 MIM$^{-/-}$ mice developed impaired IgM antibody responses to NP-FICOLL, but normal responses to
658 NP-KLH immunization, indicating that the defects were specific to the nature of the encountered
659 antigen. FICOLL polysaccharide haptenated with NP is a typical TI type 2 antigen, to which the
660 response is thought to rely mainly on marginal zone B cells and peritoneal cavity B1b cells (Guinamard

661 et al., 2000; Girkontaite et al., 2001; Hsu et al., 2006; Haas, 2011). As MIM$^{-/-}$ mice showed normal
662 proportions of peritoneal and even elevated MZ B cell compartments (Fig. 1F, G), inadequate numbers
663 of these B cell populations are unlikely to be responsible for the reduced anti-NP IgM levels (Fig, 4C).
664 However, further studies will be required to assess the functionality of B1 and MZ B cells in more
665 detail. We consider the defects in possible indirect T cell help unlikely, due to the low expression of
666 MIM in T cells (Yu et al., 2012), normal CD4^{+} T cell numbers (Fig. 1E), intact antibody responses to
667 TD antigen NP-KLH (Suppl. Fig. S4) as well as comparable levels of class-switched IgG antibodies in
668 response to NP-FICOLL immunization (Suppl. Fig. S5). We suggest that the impaired NP-FICOLL
669 responses in MIM$^{-/-}$ mice are caused by defected B cell receptor-mediated signaling, induced by cell
670 surface-associated FICOLL molecules. This would be in line with the prevailing idea that *in vivo* B cells
671 recognize and respond to antigens that are immobilized on the surface of other cells in the secondary
672 lymphoid organs (Carrasco and Batista, 2007). In case of NP-KLH stimulation these defects could be
673 rescued by second signals, to which, based on our data, MIM$^{-/-}$ cells respond well (Fig 5, Suppl. Fig. S5,
674 S6).
675
676 While naive, resting B cells have a considerably low metabolic profile, they elevate their metabolic
677 rates upon activation, which typically manifested by an increase in oxygen consumption and glycolysis
678 (Caro-Maldonado et al., 2014; Akkaya et al., 2018; Jellusova, 2018; Price et al., 2018). The mitogenic
679 stimuli IgM, LPS and CpG have been shown to dramatically increase metabolic requirements in B cells,
680 playing a key role in this transition, essential for differentiation into antibody secreting cells and
681 productive immune responses (Boothby and Rickert, 2017; Jellusova, 2018).
682
683 Our results suggest that MIM plays a negative role in metabolic reprogramming of B cells towards
684 oxidative metabolic activity upon TLR4 and especially TLR9 engagement as we found that MIM$^{-/-}$ B
685 cells exhibited ~20% increased metabolic activity after stimulation with either LPS or CpG, respective
686 agonists for TLR4 and TLR9 (Fig. 5). In contrast, basal OCR levels upon activation with anti-IgM + IL-
687 4 were reduced in MIM$^{-/-}$ cells reflecting impaired BCR signaling observed in these cells. It is possible
688 that STAT6-signaling triggered by IL-4 present in culture to increase the survival of the cells dilutes the
689 effects of defected anti-IgM signaling in MIM$^{-/-}$ cells, and leads to underestimate of the difference, as
690 IL-4 alone lead to increased metabolic activity in MIM$^{-/-}$ cells.
691
692 How exactly the impaired BCR signaling and abnormal metabolic rewiring of MIM$^{-/-}$ B cells in
693 response to TLR engagement can be explained together is an intriguing question. Surprisingly, addition
694 of BCR engagement at the same time with TLR agonists was found to negate the metabolic phenotype
695 found in MIM$^{-/-}$ B cells treated with TLR agonists alone. This suggests that increased metabolic
696 capacity in MIM$^{-/-}$ cells could compensate the effects of compromised BCR signaling upon *in vivo* B cell
697 activation and differentiation. However, how the different combinations of ligands are sensed by both
698 BCR and TLRs presents complex and largely unresolved issues. In addition to distinct modes of BCR
699 signaling induced by soluble or surface-tethered ligands, responses to simultaneous but unlinked BCR +
700 TLR stimulations are qualitatively different from co-engagement of BCR and TLR by cross-linked
701 ligands (Minguet et al., 2008; Sindhava et al., 2017). Thus, the exact mechanism of how MIM affects
702 oxidative metabolic activity in response to TLR-mediated reprograming remains to be further
703 investigated. There is, however, a large body of evidence showing that in B cells, TLR4/9-mediated
704 responses are dependent on BCR signaling components, including BCR itself (Dye et al., 2007; Minguet
705 et al., 2008; Jabara et al., 2012; Otipoby et al., 2015; Morbach et al., 2016; Schweighoffer et al., 2017;
706 Sindhava et al., 2017; Suthers and Sarantopoulos, 2017). Yet, although MIM$^{-/-}$ cells were defected in
707 activation of CD19, PI3K, Syk, Btk, NF-κB and MAPK1/2 phosphorylation upon antigenic activation,
708 we observed no abnormalities in proliferation of MIM$^{-/-}$ B cells in response to either LPS or CpG
709 (Suppl. Fig. S5E and data not shown). In the case of CpG, defects in Dock8-Src-Syk-STAT3 (Jabara et
710 al., 2012) and PI3K/Akt-GSK3b-Foxo1 (Otipoby et al., 2015) axes primarily manifest as problems in

711 proliferation. Inhibition of these modules, as well as MyD88-Pyk2-Lyn and CD19-PI3K-Akt (Morbach
712 et al., 2016), in CpG-activated cells, however, leaves activation of NF-κB and MAPK1/2 largely intact.
713 Thus, NF-κB and MAPK1/2 possess, at least partially, independent roles in TLR9 activation and may be
714 responsible for the metabolic changes seen in CpG-activated MIM$^{-/-}$ B cells. Indeed, NF-κB has been
715 shown to reduce mitochondrial oxidative metabolism in sarcoma cells and MAPK1/2 have been shown
716 to promote glycolytic shift in some cancer types, as well as in rapidly proliferating cells (Londhe et al.,
717 2018; Papa et al., 2019). This suggests that impaired activation of these modules may underpin the
718 elevated oxidative metabolism in MIM$^{-/-}$ B cells. Supporting the complex relationship of metabolism
719 with BCR and other activatory signals, it has been found that while BCR signaling initially leads to
720 enhanced mitochondrial function, this response also rapidly shifts towards mitochondrial dysfunction if
721 not rescued with second signals such as TLR9 agonists (Akkaya et al., 2018). Akkaya and colleagues did
722 not study the effects of IL-4 in this context, but it seems plausible that similar rescue of the BCR-
723 induced mitochondrial dysfunction also takes places upon IL-4 treatment. Interestingly, it has also been
724 found, that although many B cell lymphomas depend on intact tonic or antigen-driven BCR signaling, a
725 subset of diffuse large B cell lymphomas (DLBCL), called OxPhos DLBCL, with gene expression
726 signature enriched in oxidative phosphorylation genes, does not express functional BCR (Caro et al.,
727 2012; Ricci and Chiche, 2018) pointing towards separation of these signal pathways. It remains to be
728 seen if differential expression of MIM in different cancers, including lymphomas, may correlate with
729 changes in the metabolic activity of the cancer cells.
730
731
732

5 Acknowledgements

We are thankful for Laura Grönfors for technical assistance, Elmeri Kiviluoto for assistance in image analysis, Dr Maria Georgiadou and Prof Johanna Ivaska for their help and generosity with Seahorse assays, as well as Dr Diana Toivola and Joel Nyström for their help and generosity regarding the reagents for studying mitochondria. Central Animal Laboratory of University of Turku is acknowledged for good care of the mice. We thank Tero Vahlberg from the Biostatistics unit, University of Turku for his advice on statistical analysis. We thank Laboratory of Electron Microscopy at the Institute of Biomedicine, University of Turku. Microscopy and flow cytometry were performed at the Turku Bioscience Cell Imaging and Cytometry core facility, supported by Turku Bioimaging and Euro-Bioimaging consortiums. We thank the personnel for their generous help and expertise. Biocenter Finland is acknowledged for providing the research infrastructures, particularly for cell imaging and cytometry, and electron microscopy.

This manuscript has been released as a Pre-Print at BioRxiv.
doi: https://doi.org/10.1101/782276

6 Author Contributions

AS and PM designed the study. AS, PP, SHP, VŠ, EK, RV, MV and LC designed and performed the experiments. AS, PP, SHP, LC, MF, YC and PM analyzed the data. PM, YC and MF carried out supervision and provided resources for the project. AS and PM were in charge of writing the manuscript. Additionally, PP, SHP, LC, MF and YC contributed to the text.

7 Conflict of Interest

Authors declare no conflict of interest.

8 Funding

This work was supported by the Academy of Finland (grant ID: 25700, 296684, 307313, and 327378 to PM; 286712 to VŠ), Sigrid Juselius and Jane and Aatos Erkko foundations (to PM), Turku doctoral programme in molecular medicine (TuDMM) (to SHP and MV). Magnus Ehrnrooth (to AS) and Finnish Cultural (to VŠ) foundations. MF and LC were supported by the Wellcome Trust (212343/Z/18/Z) and EPSRC (EP/S004459/1).

765 **9 References**

766 Akkaya, M., Traba, J., Roesler, A. S., Miozzo, P., Akkaya, B., Theall, B. P., et al. (2018). Second signals rescue B cells from
767 activation-induced mitochondrial dysfunction and death. *Nat. Immunol.* 19, 871–884. doi:10.1038/s41590-018-0156-5.
768 Bekeredjian-Ding, I., and Jego, G. (2009). Toll-like receptors - sentries in the B-cell response. *Immunology* 128, 311–323.
769 doi:10.1111/j.1365-2567.2009.03173.x.
770 Bolger-Munro, M., Choi, K., Scurll, J. M., Abraham, L., Chappell, R. S., Sheen, D., et al. (2019). Arp2/3 complex-driven
771 spatial patterning of the BCR enhances immune synapse formation, BCR signaling and cell activation. *Elife* 8.
772 doi:10.7554/eLife.44574.
773 Boothby, M., and Rickert, R. C. (2017). Metabolic Regulation of the Immune Humoral Response. *Immunity*.
774 doi:10.1016/j.immuni.2017.04.009.
775 Bosticardo, M., Marangoni, F., Aiuti, A., Villa, A., and Grazia Roncarolo, M. (2009). Recent advances in understanding the
776 pathophysiology of Wiskott-Aldrich syndrome. *Blood* 113, 6288–95. doi:10.1182/blood-2008-12-115253.
777 Cao, M., Zhan, T., Ji, M., and Zhan, X. (2012). Dimerization is necessary for MIM-mediated membrane deformation and
778 endocytosis. *Biochem. J.* 446, 469–75. doi:10.1042/BJ20120329.
779 Caro-Maldonado, A., Wang, R., Nichols, A. G., Kuraoka, M., Milasta, S., Sun, L. D., et al. (2014). Metabolic reprogramming
780 is required for antibody production that is suppressed in anergic but exaggerated in chronically BAFF-exposed B cells.
781 *J. Immunol.* 192, 3626–36. doi:10.4049/jimmunol.1302062.
782 Caro, P., Kishan, A. U., Norberg, E., Stanley, I. A., Chapuy, B., Ficarro, S. B., et al. (2012). Metabolic Signatures Uncover
783 Distinct Targets in Molecular Subsets of Diffuse Large B Cell Lymphoma. *Cancer Cell* 22, 547–560.
784 doi:10.1016/j.ccr.2012.08.014.
785 Carrasco, Y. R., and Batista, F. D. (2007). B cells acquire particulate antigen in a macrophage-rich area at the boundary
786 between the follicle and the subcapsular sinus of the lymph node. *Immunity* 27, 160–71.
787 doi:10.1016/j.immuni.2007.06.007.
788 Carrasco, Y. R., Fleire, S. J., Cameron, T., Dustin, M. L., and Batista, F. D. (2004). LFA-1/ICAM-1 Interaction Lowers the
789 Threshold of B Cell Activation by Facilitating B Cell Adhesion and Synapse Formation. *Immunity* 20, 589–599.
790 doi:https://doi.org/10.1016/S1074-7613(04)00105-0.
791 Coughlin, J. J., Stang, S. L., Dower, N. A., and Stone, J. C. (2005). RasGRP1 and RasGRP3 Regulate B Cell Proliferation by
792 Facilitating B Cell Receptor-Ras Signaling. *J. Immunol.* 175, 7179 LP – 7184. doi:10.4049/jimmunol.175.11.7179.
793 Depoil, D., Fleire, S., Treanor, B. L., Weber, M., Harwood, N. E., Marchbank, K. L., et al. (2008). CD19 is essential for B
794 cell activation by promoting B cell receptor-antigen microcluster formation in response to membrane-bound ligand.
795 *Nat. Immunol.* 9, 63–72. doi:10.1038/ni1547.
796 Dillard, P., Varma, R., Sengupta, K., and Limozin, L. (2014). Ligand-Mediated Friction Determines Morphodynamics of
797 Spreading T Cells. *Biophys. J.* 107, 2629–2638. doi:10.1016/j.bpj.2014.10.044.
798 Dye, J. R., Palvanov, A., Guo, B., and Rothstein, T. L. (2007). B Cell Receptor Cross-Talk: Exposure to Lipopolysaccharide
799 Induces an Alternate Pathway for B Cell Receptor-Induced ERK Phosphorylation and NF-κB Activation. *J. Immunol.*
800 179, 229–235. doi:10.4049/jimmunol.179.1.229.
801 Fahrenkamp, D., Herrmann, O., Koschmieder, S., Brümmendorf, T. H., and Schemionek, M. (2017). Mtss1(CSC156) mutant
802 mice fail to display efficient Mtss1 protein depletion. *Leukemia*. doi:10.1038/leu.2017.19.
803 Girkontaite, I., Missy, K., Sakk, V., Harenberg, A., Tedford, K., Pötzel, T., et al. (2001). Lsc is required for marginal zone B
804 cells, regulation of lymphocyte motility and immune responses. *Nat. Immunol.* 2, 855–862. doi:10.1038/ni0901-855.
805 Grakoui, A., Bromley, S. K., Sumen, C., Davis, M. M., Shaw, A. S., Allen, P. M., et al. (1999). The immunological synapse:
806 a molecular machine controlling T cell activation. *Science* 285, 221–227. doi:10.1126/science.285.5425.221.
807 Guinamard, R., Okigaki, M., Schlessinger, J., and Ravetch, J. V. (2000). Absence of marginal zone B cells in Pyk-2–deficient
808 mice defines their role in the humoral response. *Nat. Immunol.* 1, 31–36. doi:10.1038/76882.
809 Haas, K. M. (2011). Programmed Cell Death 1 Suppresses B-1b Cell Expansion and Long-Lived IgG Production in Response
810 to T Cell-Independent Type 2 Antigens. *J. Immunol.* 187, 5183–5195. doi:10.4049/jimmunol.1101990.
811 Harwood, N. E., and Batista, F. D. (2010). Early events in B cell activation. *Annu. Rev. Immunol.* 28, 185–210.
812 doi:10.1146/annurev-immunol-030409-101216.
813 Hsu, M.-C., Toellner, K.-M., Vinuesa, C. G., and Maclennan, I. C. M. (2006). B cell clones that sustain long-term
814 plasmablast growth in T-independent extrafollicular antibody responses. *Proc. Natl. Acad. Sci. U. S. A.* 103, 5905–10.
815 doi:10.1073/pnas.0601502103.
816 Jabara, H. H., McDonald, D. R., Janssen, E., Massaad, M. J., Ramesh, N., Borzutzky, A., et al. (2012). DOCK8 functions as
817 an adaptor that links TLR-MyD88 signaling to B cell activation. *Nat. Immunol.* 13, 612–620. doi:10.1038/ni.2305.
818 Jellusova, J. (2018). Cross-talk between signal transduction and metabolism in B cells. *Immunol. Lett.* 201, 1–13.
819 doi:10.1016/j.imlet.2018.11.003.
820 Ketchum, C., Miller, H., Song, W., and Upadhyaya, A. (2014). Ligand mobility regulates B cell receptor clustering and
821 signaling activation. *Biophys. J.* 106, 26–36. doi:10.1016/j.bpj.2013.10.043.
822 Kuokkanen, E., Šuštar, V., and Mattila, P. K. (2015). Molecular control of B cell activation and immunological synapse
823 formation. *Traffic* 16, 311–26. doi:10.1111/tra.12257.
824 Lee, A. M., Colin-York, H., and Fritzsche, M. (2017). CalQuo 2 : Automated Fourier-space, population-level quantification

825 of global intracellular calcium responses. *Sci. Rep.* 7, 1–11. doi:10.1038/s41598-017-05322-z.
826 Lee, S. H., Kerff, F., Chereau, D., Ferron, F., Klug, A., and Dominguez, R. (2007). Structural basis for the actin-binding
827 function of missing-in-metastasis. *Structure* 15, 145–55. doi:10.1016/j.str.2006.12.005.
828 Li, L., Baxter, S. S., Gu, N., Ji, M., and Zhan, X. (2017). Missing-in-metastasis protein downregulates CXCR4 by promoting
829 ubiquitylation and interaction with small Rab GTPases. *J. Cell Sci.* 130, 1475–1485. doi:10.1242/jcs.198937.
830 Lin, J., Liu, J., Wang, Y., Zhu, J., Zhou, K., Smith, N., et al. (2005). Differential regulation of cortactin and N-WASP-
831 mediated actin polymerization by missing in metastasis (MIM) protein. *Oncogene* 24, 2059–66.
832 doi:10.1038/sj.onc.1208412.
833 Liu, C., Miller, H., Orlowski, G., Hang, H., Upadhyaya, A., and Song, W. (2012). Actin reorganization is required for the
834 formation of polarized B cell receptor signalosomes in response to both soluble and membrane-associated antigens. *J.*
835 *Immunol.* 188, 3237–46. doi:10.4049/jimmunol.1103065.
836 Londhe, P., Yu, P. Y., Ijiri, Y., Ladner, K. J., Fenger, J. M., London, C., et al. (2018). Classical NF-κB metabolically
837 reprograms sarcoma cells through regulation of hexokinase 2. *Front. Oncol.* 8. doi:10.3389/fonc.2018.00104.
838 Luxembourg, A. T., Brunmark, A., Kong, Y., Jackson, M. R., Peterson, P. A., Sprent, J., et al. (1998). Requirements for
839 Stimulating Naive CD8+ T Cells via Signal 1 Alone. *J. Immunol.* 161, 5226 LP – 5235. Available at:
840 http://www.jimmunol.org/content/161/10/5226.abstract.
841 Machesky, L. M., and Johnston, S. A. (2007). MIM: a multifunctional scaffold protein. *J. Mol. Med. (Berl).* 85, 569–76.
842 doi:10.1007/s00109-007-0207-0.
843 Mattila, P. K., Batista, F. D., and Treanor, B. (2016). Dynamics of the actin cytoskeleton mediates receptor cross talk: An
844 emerging concept in tuning receptor signaling. *J. Cell Biol.* 212, 267–280. doi:10.1083/jcb.201504137.
845 Mattila, P. K., Feest, C., Depoil, D., Treanor, B., Montaner, B., Otipoby, K. L., et al. (2013). The actin and tetraspanin
846 networks organize receptor nanoclusters to regulate B cell receptor-mediated signaling. *Immunity* 38, 461–74.
847 doi:10.1016/j.immuni.2012.11.019.
848 Mattila, P. K., Pykäläinen, A., Saarikangas, J., Paavilainen, V. O., Vihinen, H., Jokitalo, E., et al. (2007). Missing-in-
849 metastasis and IRSp53 deform PI(4,5)P2-rich membranes by an inverse BAR domain-like mechanism. *J. Cell Biol.*
850 176, 953–64. doi:10.1083/jcb.200609176.
851 Mattila, P. K., Salminen, M., Yamashiro, T., and Lappalainen, P. (2003). Mouse MIM, a Tissue-specific Regulator of
852 Cytoskeletal Dynamics, Interacts with ATP-Actin Monomers through Its C-terminal WH2 Domain. *J. Biol. Chem.* 278,
853 8452–8459. doi:10.1074/jbc.M212113200.
854 Mérida, I., Carrasco, S., and Avila-Flores, A. (2010). "Diacylglycerol Signaling: The C1 Domain, Generation of DAG, and
855 Termination of Signals," in *Protein Kinase C in Cancer Signaling and Therapy* (Totowa, NJ: Humana Press), 55–78.
856 doi:10.1007/978-1-60761-543-9_4.
857 Miettinen, T. P., and Björklund, M. (2017). Mitochondrial Function and Cell Size: An Allometric Relationship. *Trends Cell*
858 *Biol.* 27, 393–402. doi:10.1016/j.tcb.2017.02.006.
859 Minguet, S., Dopfer, E. P., Pollmer, C., Freudenberg, M. A., Galanos, C., Reth, M., et al. (2008). Enhanced B-cell activation
860 mediated by TLR4 and BCR crosstalk. *Eur. J. Immunol.* 38, 2475–87. doi:10.1002/eji.200738094.
861 Morbach, H., Schickel, J. N., Cunningham-Rundles, C., Conley, M. E., Reisli, I., Franco, J. L., et al. (2016). CD19 controls
862 Toll-like receptor 9 responses in human B cells. *J. Allergy Clin. Immunol.* 137, 889-898.e6.
863 doi:10.1016/j.jaci.2015.08.040.
864 Otero, D. C., Omori, S. A., and Rickert, R. C. (2001). CD19-dependent activation of Akt kinase in B-lymphocytes. *J. Biol.*
865 *Chem.* doi:10.1074/jbc.M003918200.
866 Otipoby, K. L., Waisman, A., Derudder, E., Srinivasan, L., Franklin, A., and Rajewsky, K. (2015). The B-cell antigen
867 receptor integrates adaptive and innate immune signals. *Proc. Natl. Acad. Sci.* 112, 12145–12150.
868 doi:10.1073/pnas.1516428112.
869 Papa, S., Choy, P. M., and Bubici, C. (2019). The ERK and JNK pathways in the regulation of metabolic reprogramming.
870 *Oncogene* 38, 2223–2240. doi:10.1038/s41388-018-0582-8.
871 Petrov, P., Sarapulov, A. V, Eöry, L., Scielzo, C., Scarfò, L., Smith, J., et al. (2019). Computational analysis of the
872 evolutionarily conserved Missing In Metastasis/Metastasis Suppressor 1 gene predicts novel interactions, regulatory
873 regions and transcriptional control. *Sci. Rep.* 9, 4155. doi:10.1038/s41598-019-40697-1.
874 Price, M. J., Patterson, D. G., Scharer, C. D., and Boss, J. M. (2018). Progressive Upregulation of Oxidative Metabolism
875 Facilitates Plasmablast Differentiation to a T-Independent Antigen. *Cell Rep.* 23, 3152–3159.
876 doi:10.1016/j.celrep.2018.05.053.
877 Ricci, J. E., and Chiche, J. (2018). Metabolic reprogramming of non-Hodgkin's B-cell lymphomas and potential therapeutic
878 strategies. *Front. Oncol.* 8, 1–23. doi:10.3389/fonc.2018.00556.
879 Saarikangas, J., Kourdougli, N., Senju, Y., Chazal, G., Segerstråle, M., Minkeviciene, R., et al. (2015). MIM-Induced
880 Membrane Bending Promotes Dendritic Spine Initiation. *Dev. Cell*. doi:10.1016/j.devcel.2015.04.014.
881 Saarikangas, J., Mattila, P. K., Varjosalo, M., Bovellan, M., Hakanen, J., Calzada-Wack, J., et al. (2011). Missing-in-
882 metastasis MIM/MTSS1 promotes actin assembly at intercellular junctions and is required for integrity of kidney
883 epithelia. *J. Cell Sci.* 124, 1245–1255. doi:10.1242/jcs.082610.
884 Safari, F., and Suetsugu, S. (2012). The BAR Domain Superfamily Proteins from Subcellular Structures to Human Diseases.

Membranes (Basel). 2, 91–117. doi:10.3390/membranes2010091.
Sarapulov, A. V, Petrov, P., Hernández-Pérez, S., Šuštar, V., Kuokkanen, E., Vainio, M., et al. (2019). Missing-In-Metastasis / Metastasis Suppressor 1 regulates B cell receptor signaling, B cell metabolic potential and T cell-independent immune responses. *bioRxiv*, 782276. doi:10.1101/782276.
Schnyder, T., Castello, A., Feest, C., Harwood, N. E., Oellerich, T., Urlaub, H., et al. (2011). B Cell Receptor-Mediated Antigen Gathering Requires Ubiquitin Ligase Cbl and Adaptors Grb2 and Dok-3 to Recruit Dynein to the Signaling Microcluster. *Immunity* 34, 905–918. doi:10.1016/j.immuni.2011.06.001.
Schweighoffer, E., Nys, J., Vanes, L., Smithers, N., and Tybulewicz, V. L. J. (2017). TLR4 signals in B lymphocytes are transduced via the B cell antigen receptor and SYK. *J. Exp. Med.* 214, 1269–1280. doi:10.1084/jem.20161117.
Shaheen, S., Wan, Z., Li, Z., Chau, A., Li, X., Zhang, S., et al. (2017). Substrate stiffness governs the initiation of B cell activation by the concerted signaling of PKCβ and focal adhesion kinase. *Elife* 6. doi:10.7554/eLife.23060.
Sindhava, V. J., Oropallo, M. A., Moody, K., Naradikian, M., Higdon, L. E., Zhou, L., et al. (2017). A TLR9-dependent checkpoint governs B cell responses to DNA-containing antigens. *J. Clin. Invest.* 127, 1651–1663. doi:10.1172/JCI89931.
Snapper, C. M. (2018). Distinct immunologic properties of soluble versus particulate antigens. *Front. Immunol.* 9. doi:10.3389/fimmu.2018.00598.
Su, T. T., Guo, B., Kawakami, Y., Sommer, K., Chae, K., Humphries, L. A., et al. (2002). PKC-β controls IκB kinase lipid raft recruitment and activation in response to BCR signaling. *Nat. Immunol.* 3, 780–786. doi:10.1038/ni823.
Suthers, A. N., and Sarantopoulos, S. (2017). TLR7/TLR9- and B cell receptor-signaling crosstalk: Promotion of potentially dangerous B Cells. *Front. Immunol.* 8, 1–8. doi:10.3389/fimmu.2017.00775.
Treanor, B., Depoil, D., Gonzalez-Granja, A., Barral, P., Weber, M., Dushek, O., et al. (2010). The membrane skeleton controls diffusion dynamics and signaling through the B cell receptor. *Immunity* 32, 187–99. doi:10.1016/j.immuni.2009.12.005.
Woodings, J. A., Sharp, S. J., and Machesky, L. M. (2003). MIM-B, a putative metastasis suppressor protein, binds to actin and to protein tyrosine phosphatase delta. *Biochem. J.* 371, 463–71. doi:10.1042/BJ20021962.
Young, R. M., and Staudt, L. M. (2013). Targeting pathological B cell receptor signalling in lymphoid malignancies. *Nat. Rev. Drug Discov.* 12, 229–43. doi:10.1038/nrd3937.
Yu, D., Zhan, X. H., Niu, S., Mikhailenko, I., Strickland, D. K., Zhu, J., et al. (2011). Murine missing in metastasis (MIM) mediates cell polarity and regulates the motility response to growth factors. *PLoS One* 6, e20845. doi:10.1371/journal.pone.0020845.
Yu, D., Zhan, X. H., Zhao, X. F., Williams, M. S., Carey, G. B., Smith, E., et al. (2012). Mice deficient in MIM expression are predisposed to lymphomagenesis. *Oncogene* 31, 3561–8. doi:10.1038/onc.2011.509.
Zhan, T., Cao, C., Li, L., Gu, N., Civin, C. I., and Zhan, X. (2016). MIM regulates the trafficking of bone marrow cells via modulating surface expression of CXCR4. *Leukemia* 30, 1327–1334. doi:10.1038/leu.2016.39.
Zhao, P., Chen, B., Li, L., Wu, H., Li, Y., Shaneen, B., et al. (2019). Missing-in-metastasis protein promotes internalization of magnetic nanoparticles via association with clathrin light chain and Rab7. *Biochim. Biophys. Acta - Gen. Subj.* 1863, 502–510. doi:10.1016/j.bbagen.2018.12.002.

924 **Figure legends**

925 **Figure 1. Largely normal B cell development and composition of B cell compartments in the bone**
926 **marrow, spleen and peritoneal cavity of MIM$^{-/-}$ mice.**
927 **(A)** Equal numbers of WT and MIM-KO splenic B cells were lysed and analyzed by immunoblotting
928 with MTSS1 antibodies (4385S (Ab #1), 4386S (Ab #2), Cell Signaling Technology). Arrowhead
929 indicates the position of the band corresponding to MIM. **(B)** Bone marrow, spleen and peritoneal cavity
930 cell populations from WT and MIM$^{-/-}$ mice were extracted for analysis by flow cytometry (C-G) using
931 the gating strategy shown in Supplementary Fig. S1 and S2. Data of 3–6 independent experiments is
932 shown as mean ± SEM. **(C)** Percentages of total CD19^{+}, CD19^{+} IgM^{+} and CD19^{-} CD117^{+} cells in the
933 bone marrow. **(D)** Percentages of B cell precursor and mature recirculating B cell populations in the
934 bone marrow. Progression through consecutive B cell developmental stages was analyzed based on the
935 major surface phenotypic markers shown in the schematic below. Percentage of corresponding bone
936 marrow populations are shown as mean ± SEM. **(E)** Percentages of CD19^{+} B cells and total (upper
937 panel) as well as CD4^{+} and CD8^{+} T cell populations (lower panel) in the spleen. (**F)** Percentages of
938 major B cell subsets in the spleen. T1–3 (transitional 1–3), Fo (follicular), MZ (marginal zone) B cells
939 are analyzed. (**G)** Percentages of CD23^{-}CD5^{+} (B1a), CD23^{-}CD5^{-} (B1b), CD23^{+}CD5^{-} (B2) B cells in the
940 peritoneal cavity.
941

942 **Figure 2. MIM deficiency leads to impaired B cell receptor signaling in response to surface-bound**
943 **antigen.**
944 **(A)** Flow cytometry analysis of Ca^{2+} mobilization in response to BCR stimulation in solution. Splenic B
945 cells from WT or MIM-KO mice were labeled with Fluo-4 and Fura Red and stimulated with 10, 5, 2.5
946 or 1 µg/mL anti-IgM antibodies. Time of anti-IgM antibody addition is indicated by an arrow. Data is
947 presented as a ratio of Fluo-4 to Fura Red median fluorescence intensity. Mean values of 3-5
948 independent experiments are shown. **(B)** Splenic B cells were stimulated on surfaces coated with
949 5 µg/mL anti-IgM antibodies for 0, 3, 7 and 15 min and lysed. Lysates were subjected for
950 immunoblotting for phosphorylated forms of different BCR signaling effector proteins.
951 Unphosphorylated forms of the corresponding proteins were used as loading control, except for pCD19,
952 pBtk and pPI3K, where NF-κB p65, Syk or Akt were used as loading controls. **(C)** Quantification of the
953 data in (B). Data is presented as ratios of phosphorylated forms to total protein levels and normalized to
954 the level of WT at 0 min. Data is from 4–8 independent experiments. Mean ± SEM is shown. * $p<0.05$,
955 ** $p< 0.01$, *** $p< 0.001$.
956

957 **Figure 3. MIM$^{-/-}$ B cells show diminished spreading and signaling on antigen-coated glass, but**
958 **gather normal levels of antigen on supported lipid bilayers.**
959 **(A)** Scanning electron micrographs of WT and MIM-KO splenic B cells at resting state, let to adhere on
960 CellTak-coated coverslips, or let to spread and get activated on coverslips coated with 5 µg/mL anti-IgM
961 for 10 min. Scale bar, 1 µm. **(B)** Splenic B cells were stimulated on coverslips coated with 7.5 µg/mL
962 anti-IgM antibodies for 10 min, fixed, permeabilized and stained with phalloidin (F-actin) and anti-
963 phospho-Tyrosine antibodies (pTyr). Samples were imaged with TIRF microscopy. Representative
964 images showing cell spreading and F-actin staining, are shown (upper left). Area of spreading was
965 analyzed by signal thresholding in pTyr channel (lower left panels), and pTyr (upper right panels) and F-
966 actin (lower right panels) intensities inside cell perimeter were quantified using ImageJ. Mean (MFI) and
967 total (total) fluorescence intensities of pTyr and F-actin stainings are shown, and the mean fluorescence
968 intensity is presented both as pairwise comparison of geometric means of individual experiments (on the
969 left) and as scatter plots of random sampling of 92 cells from each of 3-4 individual experiments
970 (middle). Mean ± SEM is shown. Scale bar, 5 µm. **(C)** Splenic B cells were stimulated on coverslips
971 coated with 5 µg/mL anti-IgM antibodies for 3, 5, 7, 10 and 15 min, fixed, permeabilized and stained
972 with phalloidin (F-actin) and anti-phospho-Btk (pBtk) or anti-phospho-Syk (pSyk) antibodies. Samples
973 were imaged with spinning disk confocal microscopy. Area of spreading was analyzed by signal

974 thresholding in phalloidin channel, and pBtk or pSyk mean fluorescence intensities (MFI) inside cell
975 perimeter were quantified using ImageJ and normalized to non-activated cells (time 0 min). Normalized
976 MFI of pBtk and pSyk, and spreading area based on F-actin are shown. Data is shown as mean ± SEM
977 of 4 independent experiments (~25-150 cells per condition per experiment). WT and KO cells were
978 compared using unpaired t-test. **(D)** Intracellular Ca^{2+}-flux was analyzed in splenic WT and MIM-KO B
979 cells loaded with Fluo-4 and stimulated with anti-kappa light chain antibodies tethered on supported
980 lipid bilayers (SLB). A spinning disk confocal microscope was used to record the Fluo-4 intensity and
981 the intracellular Ca^{2+} levels were quantified with *CalQuo*[2] software. Representative images of stimulated
982 B cells, 85 sec after injection into the chamber are shown (upper panel). Mean percentages of non-
983 triggering cells and cells with single peak or oscillatory responses are shown (lower panel). Data of 3
984 independent experiments. Scale bar, 100 µm. **(E)** Splenic WT and MIM-KO B cells were stimulated
985 with monobiotinylated anti-kappa light chain antibodies tethered via AF647-labelled streptavidin on
986 SLBs. A laser scanning confocal microscope was used to detect IRM signal (panels on the left)
987 corresponding to the area of contact and to measure the amount of antigen collected in the synapse from
988 the AF647 signal (panels on the right). The data was quantified for cell area (graphs on the left), antigen
989 area and antigen fluorescence intensity (graphs on the right) during synapse formation (0-7 min) by
990 tracking individual cells from live cell imaging movies, and in the mature synapse (>10 min) by taking
991 snapshots from several fields of views after movie acquisition. Data is from 3-4 independent
992 experiments (~25-30 cells per condition in the movie, ~400-450 cells in the snapshots). Data were
993 compared using unpaired t-test. Mean ± SEM is shown. Scale bar, 1 µm. * $p<0.05$, ** $p< 0.01$, *** $p<$
994 0.001, **** $p<0.0001$
995
996 **Figure 4. MIM-deficiency results in impaired IgM response and reduced levels of total IgGs**
997 **during T cell-independent immune response.**
998 **(A)** Basal antibody levels of major immunoglobulin subclasses were measured from 17–18 WT and
999 MIM KO mice. **(B)** A schematic representation of T cell-independent (TI) immunization study. **(C)** The
1000 antibody responses of immunized WT and MIM-KO mice were followed from serum samples as in (B).
1001 Total and NP-specific antibody levels of different immunoglobulin isotypes were measured with ELISA.
1002 7-8 mice per group. Mean ± SEM is shown. * $p<0.05$, ** $p< 0.01$.
1003
1004 **Figure 5. MIM-deficient B cells show increased metabolic activity upon stimulation with Toll-like**
1005 **receptor ligands LPS and CpG.**
1006 **(A)** Oxygen consumption rate (OCR) profiles of WT and MIM-KO splenic B cells stimulated with IL-4,
1007 anti-IgM + IL-4, LPS, CpG, anti-IgM + LPS, or anti-IgM + CpG for 24 h were measured in a Seahorse
1008 XF Cell Mito Stress Test assay. The different steps of the assay are depicted in the graph on the left
1009 showing mean ± SEM. Comparisons of baseline mitochondrial respiration as well as maximum and
1010 spare respiratory capacities, extracted from the assay, are shown in the graphs in the middle, and
1011 quantification of the ratio of OCR to extracellular acidification rate (ECAR) at the baseline is shown on
1012 the right. Data presented as mean of 4–8 independent experiments. Mean ± SEM. (**B–C**) Splenic B cells,
1013 either left unstimulated (**B**) or stimulated with LPS or CpG for 24 h (**C**), were loaded with TMRE to
1014 probe for the mitochondrial membrane potential, or stained with anti-Tom20 antibodies to derive total
1015 mitochondrial mass. The samples were analyzed by flow cytometry. Data of 3 independent experiments.
1016 Mean ± SEM. * $p<0.05$.
1017
1018

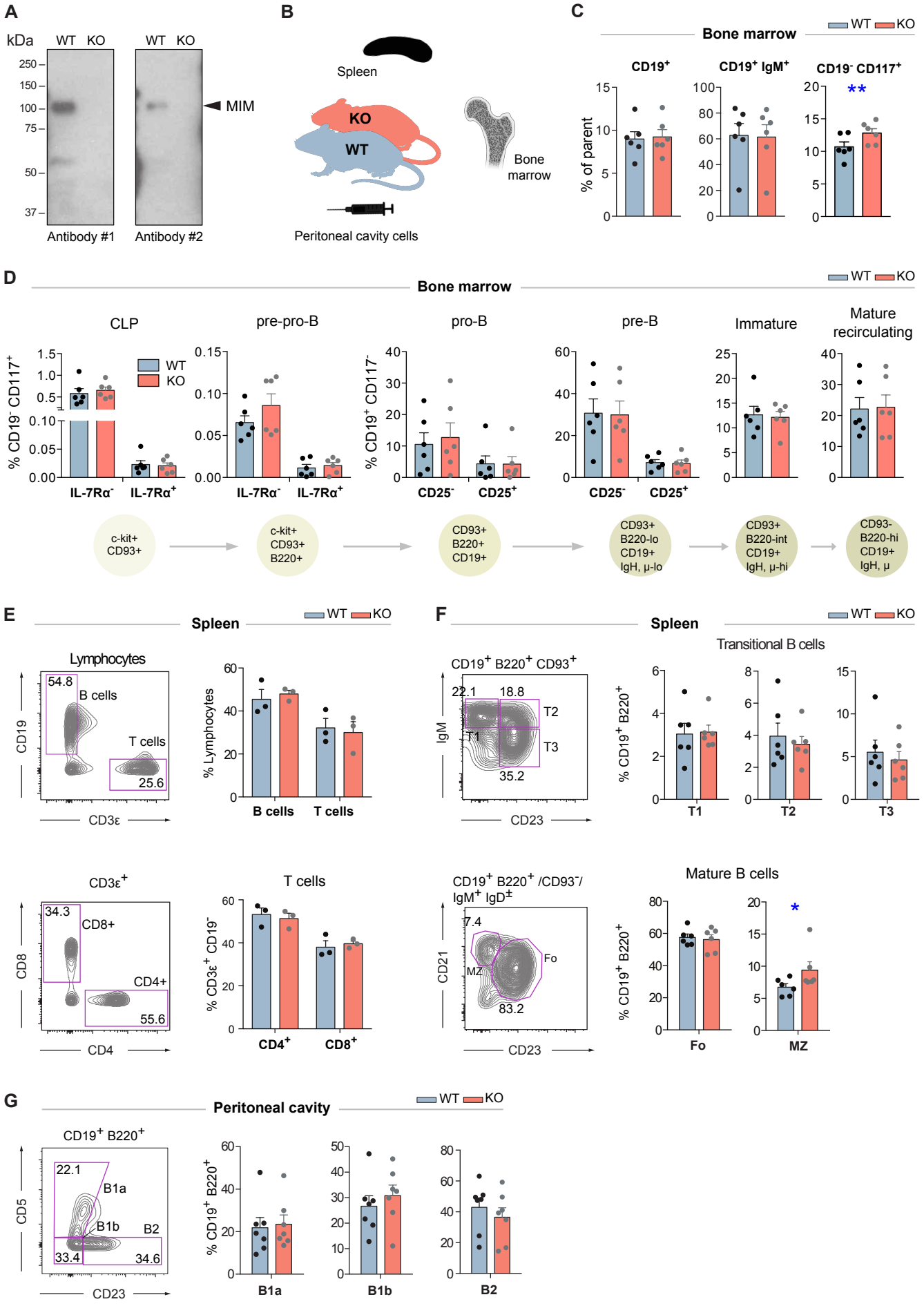
A
kDa
WT KO
WT KO
250
150
100
75
50
37
MIM
Antibody #1
Antibody #2
B
Spleen
KO
WT
Bone marrow
Peritoneal cavity cells
C
Bone marrow
WT KO
CD19+
CD19+ IgM+
CD19- CD117+
% of parent
**
D
Bone marrow
WT KO
CLP
pre-pro-B
pro-B
pre-B
Immature
Mature recirculating
% CD19- CD117+
% CD19+ CD117-
IL-7Rα-
IL-7Rα+
CD25-
CD25+
c-kit+ CD93+
c-kit+ CD93+ B220+
CD93+ B220+ CD19+
CD93+ B220-lo CD19+ IgH, μ-lo
CD93+ B220-int CD19+ IgH, μ-hi
CD93- B220-hi CD19+ IgH, μ
E
Spleen
WT KO
Lymphocytes
54.8
B cells
T cells
25.6
CD19
CD3ε
% Lymphocytes
B cells
T cells
CD3ε+
34.3
CD8+
CD4+
55.6
CD8
CD4
T cells
% CD3ε+ CD19-
CD4+
CD8+
F
Spleen
WT KO
CD19+ B220+ CD93+
22.1
18.8
T1
T2
T3
35.2
IgM
CD23
Transitional B cells
% CD19+ B220+
T1
T2
T3
CD19+ B220+ /CD93-/ IgM+ IgD±
7.4
MZ
Fo
83.2
CD21
CD23
Mature B cells
*
Fo
MZ
G
Peritoneal cavity
WT KO
CD19+ B220+
22.1
B1a
B1b
B2
33.4
34.6
CD5
CD23
% CD19+ B220+
B1a
B1b
B2

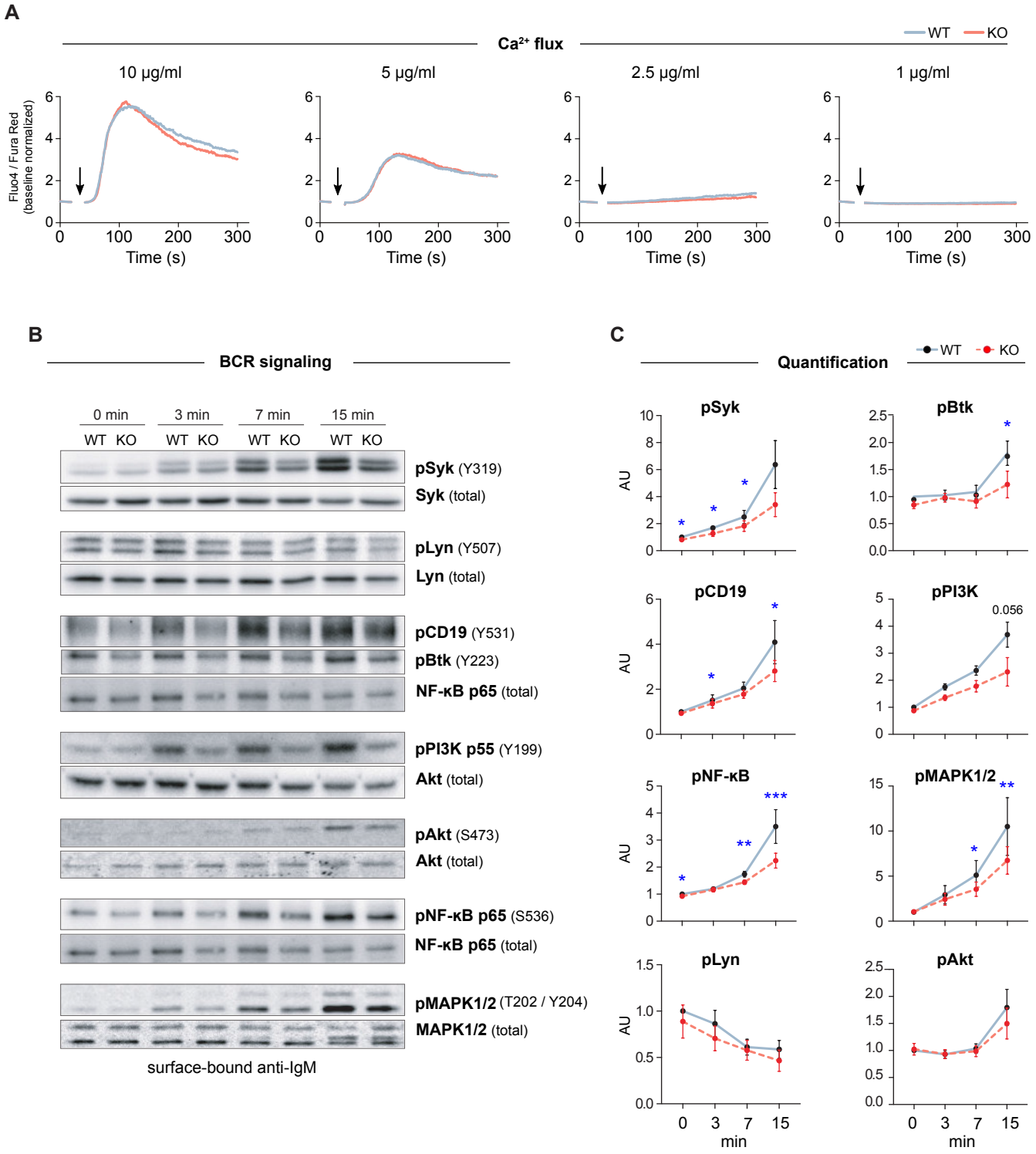
A
Ca²⁺ flux
WT
KO
10 µg/ml
5 µg/ml
2.5 µg/ml
1 µg/ml
Fluo4 / Fura Red (baseline normalized)
Time (s)
B
BCR signaling
0 min
3 min
7 min
15 min
WT KO
pSyk (Y319)
Syk (total)
pLyn (Y507)
Lyn (total)
pCD19 (Y531)
pBtk (Y223)
NF-κB p65 (total)
pPI3K p55 (Y199)
Akt (total)
pAkt (S473)
Akt (total)
pNF-κB p65 (S536)
NF-κB p65 (total)
pMAPK1/2 (T202 / Y204)
MAPK1/2 (total)
surface-bound anti-IgM
C
Quantification
pSyk
pBtk
pCD19
pPI3K
0.056
pNF-κB
pMAPK1/2
pLyn
pAkt
AU
min

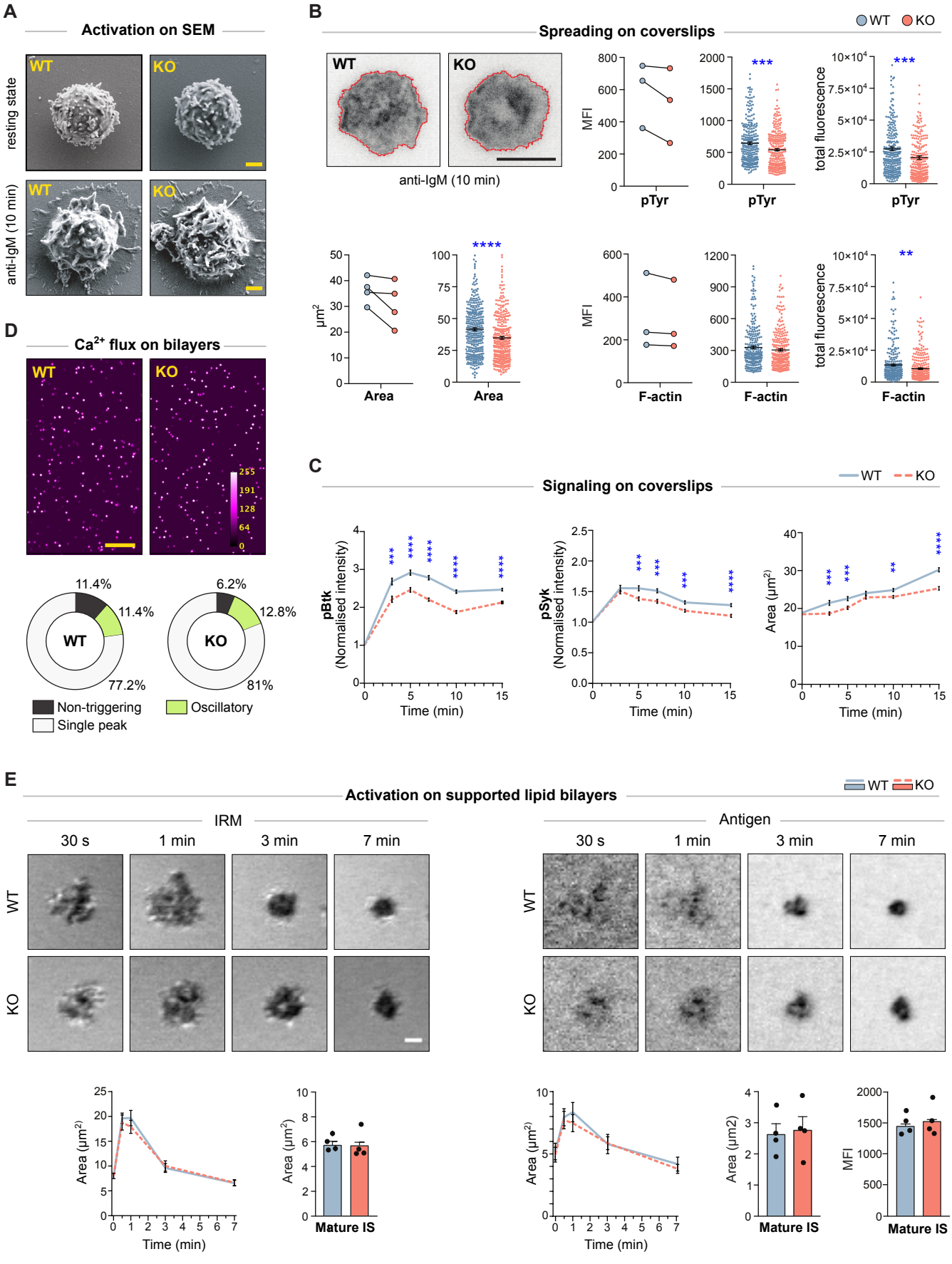
A
Activation on SEM
resting state
anti-IgM (10 min)
WT
KO
B
Spreading on coverslips
WT
KO
anti-IgM (10 min)
MFI
pTyr
total fluorescence
μm²
Area
F-actin
C
Signaling on coverslips
pBtk (Normalised intensity)
pSyk (Normalised intensity)
Area (μm²)
Time (min)
D
Ca²⁺ flux on bilayers
255
191
128
64
0
11.4%
11.4%
77.2%
6.2%
12.8%
81%
Non-triggering
Oscillatory
Single peak
E
Activation on supported lipid bilayers
IRM
Antigen
30 s
1 min
3 min
7 min
Area (μm²)
Time (min)
Mature IS
MFI

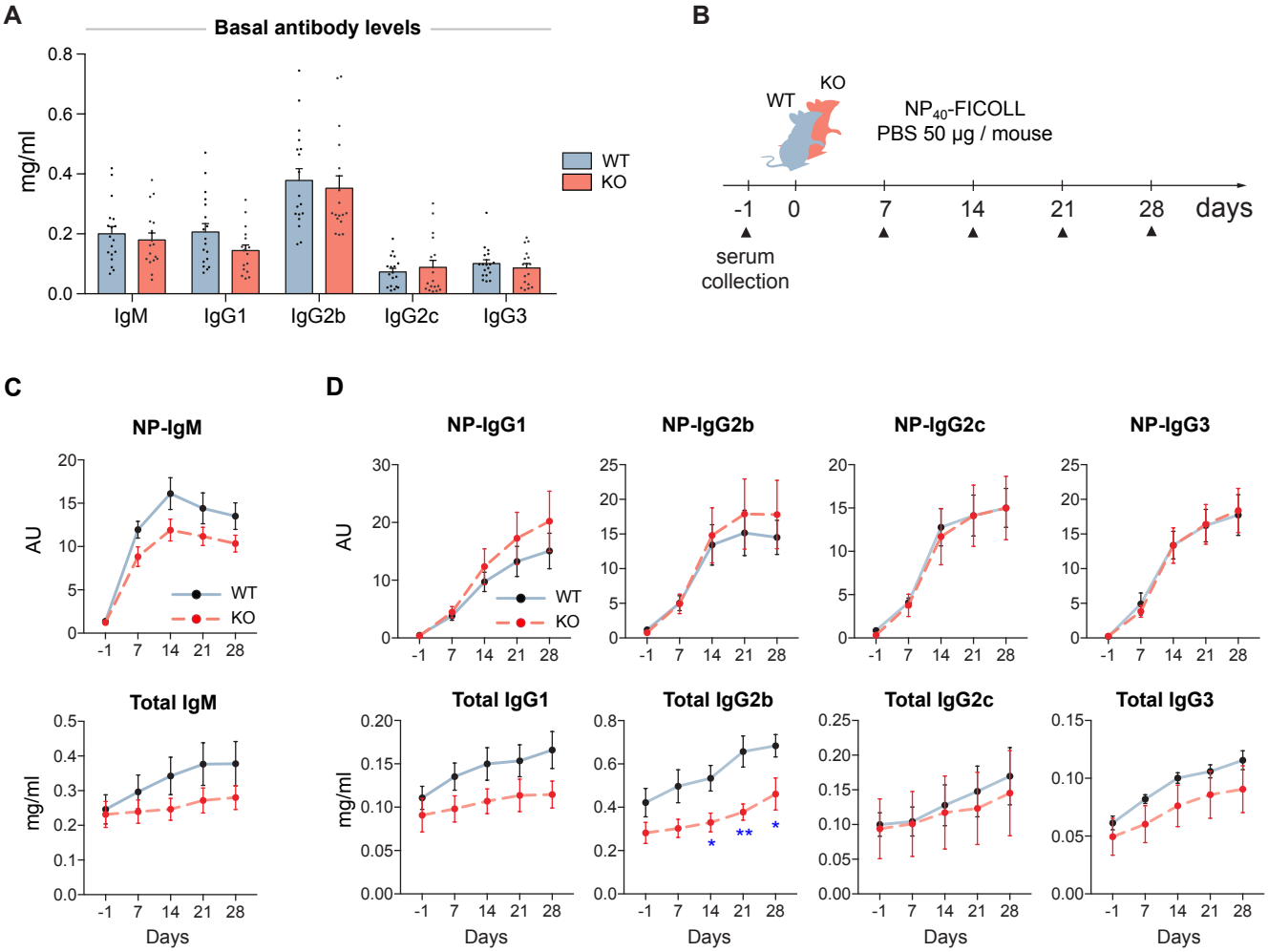
A
Basal antibody levels
mg/ml
0.8
0.6
0.4
0.2
0.0
IgM
IgG1
IgG2b
IgG2c
IgG3
WT
KO
B
WT
KO
NP40-FICOLL
PBS 50 µg / mouse
-1
0
7
14
21
28
days
serum
collection
C
NP-IgM
AU
20
15
10
5
0
WT
KO
-1
7
14
21
28
Total IgM
mg/ml
0.5
0.4
0.3
0.2
0.1
0.0
Days
D
NP-IgG1
NP-IgG2b
NP-IgG2c
NP-IgG3
AU
30
20
10
0
25
15
5
Total IgG1
Total IgG2b
Total IgG2c
Total IgG3
mg/ml
0.20
0.15
0.10
0.05
0.00
0.8
0.6
0.4
0.2
0.25
*
**

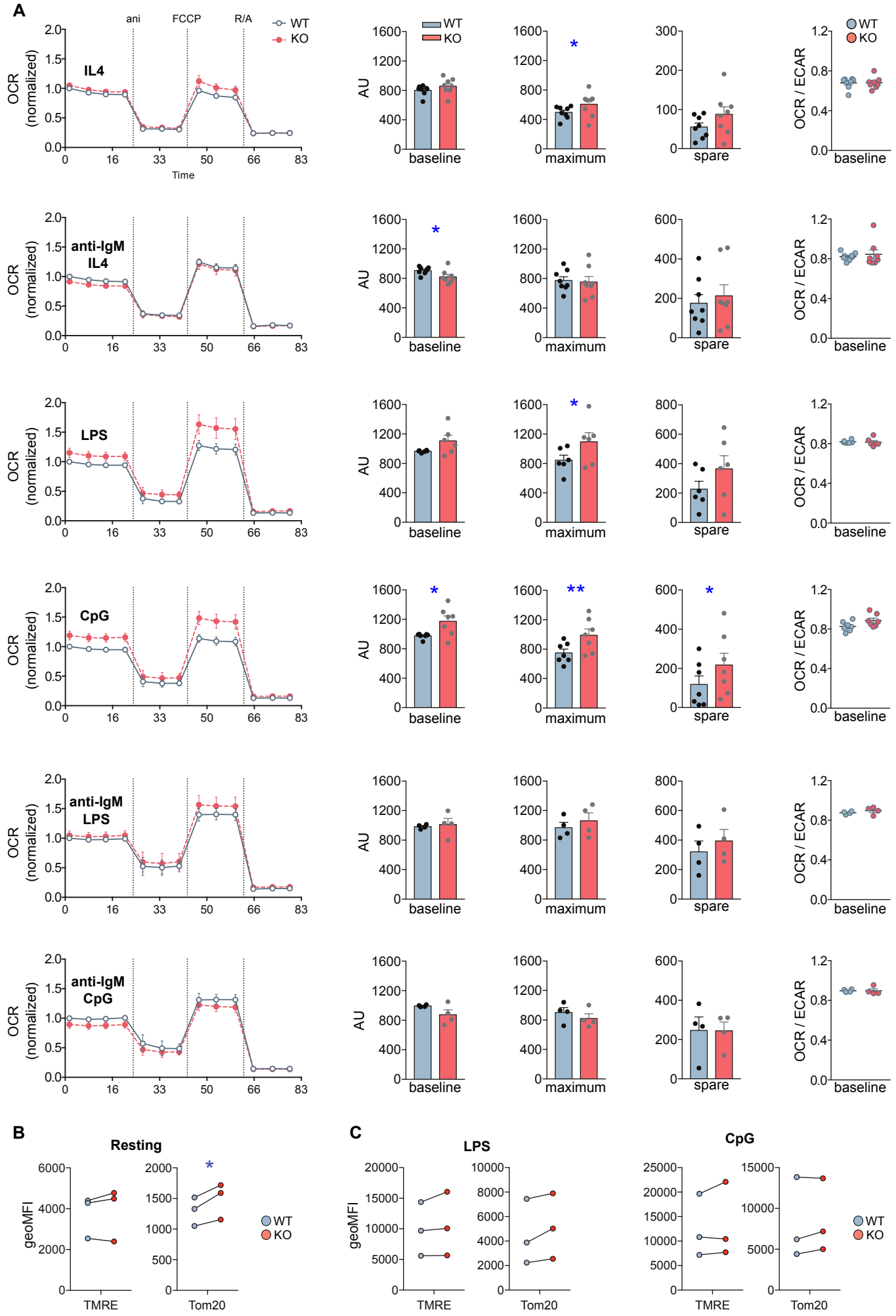
A
ani
FCCP
R/A
WT
KO
IL4
anti-IgM
IL4
LPS
CpG
anti-IgM
LPS
anti-IgM
CpG
OCR
(normalized)
Time
AU
baseline
maximum
spare
OCR / ECAR
B
Resting
geoMFI
TMRE
Tom20
C
LPS
CpG